Mon. Not. R. Astron. Soc. **286,** 558–582 (1997)

Radio, optical and X-ray observations of PKS 2250 – 41: a jet/galaxy collision?

N. E. Clark,[1] C. N. Tadhunter,[1] R. Morganti,[2,3] N. E. B. Killeen,[3] R. A. E. Fosbury,[4] R. N. Hook,[4] J. Siebert[5] and M. A. Shaw[1]

[1]*Department of Physics, University of Sheffield, Sheffield S3 7RH*
[2]*Instituto di Radioastronomia, CNR, via Gobetti 101, Bologna, Italy*
[3]*ATNF, CSIRO, PO Box 76, Epping NSW 2121, Australia*
[4]*ST-ECF/ESO, Karl-Schwarzschild-Straße 2, D-85740 Garching bei München, Germany*
[5]*Max-Planck-Institut für Extraterrestrische Physik, Giessenbachstraße, D-85740 Garching, Germany*

Accepted 1996 October 27. Received 1996 October 8; in original form 1996 May 9

ABSTRACT

New optical, radio and X-ray observations are used to investigate the morphology, ionization and kinematics of extended structures in the host galaxy of the radio source PKS 2250 – 41 ($z = 0.308$). The data provide clear evidence for a powerful interaction between the radio jets and the ambient interstellar medium. Not only do [O III] emission-line images show spectacular extended arc structures associated with the radio lobes on both sides of the galaxy nucleus on a scale of 40–65 kpc,[1] but there is also large depolarization in the western radio lobe at the position of the western emission-line arc. Optical long-slit spectra of the extended emission-line regions provide the first convincing evidence that the radio jets can have a major ionizing effect on the warm gas in powerful radio galaxies: while the low-ionization [N II] and [S II] lines are broad (FWHM $\sim$ 300–500 km s^{-1}) across the entire emission-line nebulosity, the higher ionization [O III] lines are significantly narrower in the western emission-line arc (FWHM $= 240 \pm 10$ km s^{-1}). This anticorrelation between linewidth and ionization is difficult to explain in terms of central source photoionization, but is entirely consistent with the compression or direct ionization effects of fast shocks driven by the radio jets. Further evidence for shocks is provided by the minimum in the ionization state at the position of the radio lobes, and by [O III](5007 + 4959)/4300 and He II/Hβ diagnostic ratios which are more consistent with shocks than with photoionization. The spectacular nature of the jet/cloud interaction in this object is best explained in terms of a direct collision between the radio jet and a companion galaxy in the surrounding group. This model is supported by the detection of a blue continuum source in the western arc with a colour and luminosity characteristic of late-type spiral galaxies.

Key words: galaxies: active – galaxies: interactions – galaxies: jets – radio continuum: galaxies – X-rays: galaxies.

1 INTRODUCTION

Extended emission-line regions (EELR) are observed in a large fraction of powerful radio galaxies (Tadhunter 1987; Baum et al. 1988), extending over tens of kiloparsecs, with a wide range of morphological, kinematical and spectral properties. One of the most interesting properties of the EELR is their preferential alignment along the axes of extended radio emission, which becomes more pronounced as the redshift increases (McCarthy et al. 1987; Baum & Heckman 1989). The aligned EELR have been used both as fluorescent screens to test the unified schemes for radio sources (e.g. Morganti et al. 1991) and as probes of the dynamics and mass distribution of the host galaxies (Tadhunter, Fosbury & Quinn 1989a). There is therefore much

[1]$H_0 = 50$ km s^{-1} Mpc^{-1}, $q_0 = 0.0$ used throughout, giving an angular scale of 6.0 kpc arcsec^{-1}.

interest in understanding the origins of the aligned structures, and the ionization mechanisms for the warm, emission-line gas.

Current models used to explain the aligned structures fall into two broad categories: anisotropic illumination by a central AGN, and jet/cloud interactions (see Tadhunter 1996b for a review). In the anisotropic illumination model, the EELR are photoionized by an anisotropic, ionizing nuclear-continuum source (e.g. Fosbury 1989). The extended continuum structures represent a combination of light scattered out of the radiation cones of the central AGN (Tadhunter et al. 1988b; Fabian 1989) and nebular continuum emitted by the warm emission-line clouds (Dickson et al. 1995). This model is supported by the generally good agreement between the emission-line ratios and the photoionization models (Robinson et al. 1987), and by the measurement of significant optical/UV continuum polarization in several objects (Tadhunter et al. 1992; Cimatti et al. 1993). An advantage of the anistropic illumination model is that it is consistent with the unified schemes for radio sources (e.g. Barthel 1989), which predict the required cones of ionizing radiation.

However, in some powerful radio galaxies – particularly those at high redshift – strong evidence also exists for interactions between the radio jets and the ISM/IGM. Observations reveal that the extended line emission is often not only generally aligned with the radio axis but also closely correlated in detail with the radio emission over distances of tens of kiloparsecs (e.g. van Breugel et al. 1985; Djorgovski et al. 1987; Chambers, Miley & van Breugel 1990; Miley et al. 1992). For such galaxies, the spectra of the EELR often reveal extreme kinematic components associated with the radio emission, with typical rest-frame linewidths of ~ 1000 km s^{-1} (FWHM) (McCarthy, Baum & Spinrad 1996). The manifestations of these apparently jet-induced phenomena are clearest on a scale of ~ 10–100 kpc, where there are clear morphological associations between the radio and optical features. However, the recent detection of extreme high-velocity components and line broadening in the core of the nearby powerful radio galaxy Cygnus A (Tadhunter 1991; Tadhunter, Metz & Robinson 1994a) provide evidence that the jets may also have an effect on the kpc scale in the narrow-line region, where the morphological signs of interaction are less clear.

Despite much work, the extent to which the properties of the extended emission-line structures are determined by anisotropic illumination on the one hand, and by jet/cloud interactions on the other, remains uncertain. We know that jet/cloud interactions occur, but we are far from understanding the detailed physics of such interactions.

To remedy this situation, we have begun a programme of detailed observations of low- and intermediate-redshift jet/cloud interaction candidates. Here we report the results of a comprehensive, multiwavelength study of the powerful southern source PKS 2250 – 41 ($z = 0.308$) which was observed as part of this programme.

2 PREVIOUS OBSERVATIONS

PKS 2250 – 41 ($z = 0.308$) is one of the most spectacular objects discovered in a survey of southern, 2-Jy radio galaxies (Morganti, Killeen & Tadhunter 1993; Tadhunter et al. 1993). Previous results on the emission-line, continuum and polarization properties of this source have been published by Tadhunter et al. (1994b), Dickson et al. (1995) and Shaw et al. (1995).

At radio wavelengths the source does not appear unusual, having a classical double structure characteristic of Fanaroff–Riley type II (FRII) radio sources (Duncan & Sproats 1993; Morganti et al. 1993). However, at optical wavelengths narrow-band [O III] images reveal a striking emission-line nebulosity extending along the roughly east–west axis of the radio source in a series of arc structures (Tadhunter et al. 1994). The brightest, western arc is found to circumscribe the outer edge of the western radio lobe. There is also evidence from long-slit spectroscopy observations for a link between the ionization state of the extended gas and the radio structure, with a pronounced maximum in the [O II]3727/[O III]5007 emission-line ratio close to the centroid of the western radio lobe (Tadhunter et al. 1994b).

The bright western arc is associated with a blue, optical continuum source. Imaging polarimetry observations show that, in contrast to the results obtained for the circumnuclear regions of many powerful radio galaxies at high and intermediate redshifts (Tadhunter et al. 1992), the optical polarization of this continuum source is low (< 3.5 per cent in the B band; Shaw et al. 1995). Thus Tadhunter et al. (1994b) ruled out the idea that the extended continuum is dominated by scattered AGN light, or optical synchrotron emission associated with the radio source. A recent detailed analysis of the continuum spectrum by Dickson et al. (1995) shows that a large fraction of the extended, ultraviolet light in the western arc comprises nebular continuum emitted by warm emission-line clouds. Following the subtraction of the nebular component, Dickson et al. found a residual continuum which, while redder than the original continuum, has relatively blue colours. The origin of this residual continuum is uncertain.

Given the close associations between radio and optical structures, PKS 2250 – 41 is a key object for understanding the physical mechanisms in jet/cloud interactions. We present below new radio, optical and X-ray observations, which are used to make a detailed analysis of the kinematics, ionization and origins of the extended warm gas in this important source.

3 OBSERVATIONS

3.1 Optical imaging

The optical imaging data were obtained using the European Southern Observatory Faint Object Spectrograph and Camera (EFOSC) on the ESO 3.6-m telescope at La Silla in 1993 July. A log of the observations is presented in Table 1. The Tek CCD in the EFOSC has 512×512 pixels, giving a spatial scale of 0.61 arcsec pixel^{-1}. While the broad-band images were made using standard B and V filters, the narrow-band [O III] λ5007 and [O III] continuum images were made with ESO filters no. 436 ($\lambda_0 = 6548$ Å, $\Delta\lambda = 62$ Å FWHM) and no. 442 ($\lambda_0 = 6939$ Å, $\Delta\lambda = 65$ Å FWHM) respectively. The [O III] continuum image is of low signal-to-noise and contains little useful information about the extended continuum structures. We find that subtracting

Table 1. Log of the optical imaging observations.

Date	Seeing (arc s)	Filter	Exposure Time (s)
21/7/93	1.4	B	2 x 300
22/7/93	1.4	V	2 x 300
22/7/93	1.3	[OIII]	2 x 900
22/7/93	1.3	Continuum	2 x 300

this image from the [O II] image makes little difference to the appearance of the extended structures, apart from degrading the signal-to-noise ratio. Therefore, in what follows, we present and discuss only the [O III] image which has not been continuum-subtracted.

The imaging data were reduced using standard techniques with the Starlink KAPPA package (see Shaw et al. 1995 for a complete description of the data-reduction procedure). The narrow-band [O III] and *B*-band images were presented in Tadhunter et al. (1994b). To obtain sharper images, we have restored the reduced images using the Richardson–Lucy algorithm. These images have good signal-to-noise ratio, but are approximately critically sampled. To obtain a small enhancement of contrast and resolution, they were restored on to a finer pixel grid. The background of the images was first subtracted using an algorithm which maximizes the amount of 'blackness' in the result (L. B. Lucy 1993, personal communication). 10 iterations of the Richardson–Lucy algorithm (Richardson 1972; Lucy 1974) were then applied using the ACOADD task within the STSDAS/IRAF analysis system (Hook & Lucy 1993). The resultant images were constructed on a grid with twice the original spatial sampling in both directions. The effective seeing (FWHM) of the images after restoration is 0.9 ± 0.1 arcsec, which compares with the 1.4-arcsec FWHM of the original images.

3.2 Radio observations

PKS 2250 − 41 was observed with the Australia Telescope Compact Array (ATCA) at 8 and 5 GHz. Observing at 8 GHz enabled us to achieve a resolution of ~ 1 arcsec, the highest resolution currently possible with this instrument. The observations were made on 1994 September 4, using a 6-km array configuration and the standard continuum correlator set-up providing a bandwidth of 128 MHz with 32, 4-MHz channels. The two simultaneous frequencies were set to 8.6 and 5.8 GHz. The source was observed for 6 h in total, spread out in equal length cuts over 12 h. The primary flux density calibrator (1934 − 638) was observed at the beginning, and the secondary calibrator (2254 − 367) was observed every 30 min to track the complex antenna gains with time.

The data were analysed with the MIRIAD package (Sault, Teuben & Write 1995). All images were produced with standard synthesis imaging, deconvolution (CLEAN; see Högbom 1974; Clark 1980) and self-calibration (e.g. Schwab 1980) methods. Additionally, all our images were made with uniform weighting, which provides a better synthesized beam (narrower main peak and smaller sidelobes) at the expense of some sensitivity.

3.3 Optical spectroscopy

Table 2 gives details of the long-slit spectroscopy observations which were made using both the EFOSC on the ESO 3.6-m telescope and the RGO spectrograph on the 3.9-m Anglo-Australian Telescope (AAT). The slit was oriented at PA 270° throughout. For the blue EFOSC data, the Tek CCD (512×512 pixel) gave a wavelength range of 3800–7000 Å, while in the red the Tek CCD on the RGO spectrograph (226×1024 pixel) gave a wavelength range of 5750–9220 Å. The data were reduced using the FIGARO data-reduction package. The reduction procedure consisted of bias subtraction, cosmic ray removal, flat-fielding, wavelength calibration, atmospheric extinction correction, sky subtraction and flux calibration. Steps were also taken to ensure that the wavelength and spatial directions were aligned accurately with the *x*- and *y*-axes of the CCD detectors.

Intercomparison of the blue EFOSC spectra showed that the position of the slit was not identical for all of the three CCD frames. To find the exact position of the slit for each distinct spectrum, spatial cross-sections of the narrow-band [O III] image were extracted to simulate the slit across the object. These cross-sections were compared with extracted spatial slices from each long-slit spectrum (centred on [O III] λ5007) to deduce the actual position of the slit in each case. Fig. 1 shows the derived slit positions for each spectrum, superposed on a contour plot of the narrow-band [O III] image.

Because the blue EFOSC spectra were displaced from one another, each of them was analysed separately. On the other hand, the slit positions were coincident for the red RGO spectrograph data, so the individual spectra were co-added to produce a single long-slit spectrum.

The spectra were analysed using the Starlink DIPSO spectral analysis package; single, spatial-pixel spectral slices were extracted from the long-slit spectra, and Gaussians were then fitted to the emission lines. The measured linewidths were corrected for the instrumental width – measured from the night-sky lines – using the Gaussian quadrature technique.

3.4 X-ray imaging

To gain clues to its gaseous environment, PKS 2250 − 41 was also observed with the High-Resolution Imager (HRI)

Table 2. Log of the long-slit spectroscopy observations.

Telescope	Instrument	Date	Seeing (arcsec)	Slit (arcsec)	Exposure time (s)	Pixel Scale (Å/arcsec)
ESO 3.6m	EFOSC	21 & 23/7/93	1.4-1.7	2.0	3 x 1200	0.61/6.4
AAT 3.9m	RGO Spectrograph	12/8/93	1.0-1.7	1.5	4 x 1800	0.81/3.4

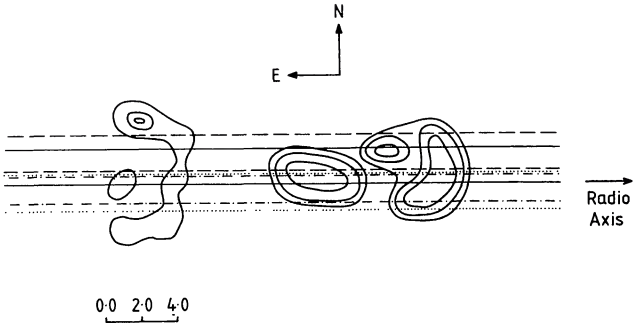

Figure 1. Sketch showing the slit positions for the long-slit spectroscopic observations of PKS 2250 – 41, superimposed on a contour representation of the narrow-band [O III] image. The location of the slit for the red observations (dot-dashed line), and the northernmost (dashed line), central (solid line) and southernmost (dotted line) blue spectra are all plotted. The orientation and spatial scale are also indicated.

of the *ROSAT* satellite in the 0.1 to 2.4 keV energy band. The total integration time of the observation was 21 028 s. The X-ray image was analysed using tasks in the MIDAS EXSAS package.

4 RESULTS

4.1 Optical images

The restored narrow-band [O III] λ5007 image (Fig. 2a) reveals several interesting features, including the following.

Extended arc structures. As noted by Tadhunter et al. (1994b) the dominant feature of the [O III] image is the prominent arc structure situated at a projected radial distance of 6.1 arcsec (37 kpc) to the west of the continuum nucleus. This arc has a total length of $\sim$8 arcsec ($\sim$50 kpc), and its brightness increases from north to south. It is spatially resolved in the restored image with a projected width (FWHM) of 1.5–1.8 arcsec (9–11 kpc). Fainter emission-line arcs are also observed to the east of the nucleus, at projected radii of 8 and 10.4 arcsec (48 and 63 kpc). The eastern arcs are clumpier, and there are gaps in both arcs slightly to the south of the east–west axis.

Fainter extended emission to the west. An important new result is the detection of a faint patch of emission outside the main western arc at a projected radius 10.6 arcsec (64 kpc). This feature is also seen in continuum-subtracted spatial emission-line profiles extracted from our long-slit spectra, and appears to be an emission-line rather than a continuum structure. The inner part of this feature has an arc structure, roughly concentric with the main western arc. Note that, while the main arcs on the east and west of the nucleus show a close association with the extended radio structures, this faint emission-line structure lies well *outside* the radio emission on the west side of the nucleus (see Section 4.2.4).

The 'X' structure. On a smaller 2–5 arcsec (15–30 kpc) scale, the emission lines form an 'X' structure centred on the continuum nucleus of the host galaxy. Part of the 'X' in the north-west direction comprises a spatially distinct clump of [O III] emission at a radius of 4.3 arcsec (26 kpc).

The nuclear ellipsoid. The EELR in the circumnuclear region (<3 arcsec or <18 kpc) have an elliptical structure with the major axis of the ellipse aligned along PA 80°. Gaussian fits to the spatial distributions of emission-line and continuum fluxes derived from our long-slit spectra show a significant spatial offset between the emission-line and continuum peaks near the nucleus, with the emission lines peaking 0.55 ± 0.03 arcsec (3.3 ± 0.2 kpc) to the east of the continuum peak.

The companion galaxy to the NE. The [O III] image also shows what appears to be a neighbouring galaxy at the northern extreme of the outermost eastern arc, at a radius of 10.6 arcsec (64 kpc) from the nucleus along PA 69°. Comparisons between the emission-line, continuum and broad-band images show that this is a predominantly continuum-emitting structure. Spectra of this structure (northernmost EFOSC spectrum) show faint [O III] λ5007 line emission at the redshift of the PKS 2250 – 41 host galaxy, possible signs of a 4000-Å continuum break at a similar redshift, and a relatively red continuum.

The structure of the extended emission in the restored broad-band *B* and *V* images (Figs 2b and c respectively) is markedly different from that seen in the [O III] image. Notably, the extended emission to the west of the nucleus is more centrally concentrated, particularly in the *B* band, and the western arc is less distinct. The broad *V*-band image also reveals possible signs of tidal tails associated with the companion galaxy to the north-east, which suggest a recent galaxy interaction. However, the broad-band images also show some similarities with the [O III] image, including the general alignment of the brighter structures along the east–west axis, the central 'X' structure, and the fainter arcs to the east of the nucleus.

One problem with interpreting the broad-band images is that the filter bandpasses include emission lines as well as continuum (see Fig. 7a). The contamination is worst for the extended arc structure, where the emission lines contribute as much as 53 per cent of the light in the *V* band and 40 per cent in the *B* band, but it is lower in the nuclear regions where the corresponding figures are 21 per cent (*V*) and 22 per cent (*B*). In spite of this emission-line contamination, it is clear that structures seen in the broad-band images are comprised partly of continuum emission. Indeed, on the western side of the nucleus the continuum is detected directly on the long-slit spectra. Also, given that the shorter exposure broad-band observations are far less sensitive to faint emission-line structures than the narrow-band images, the clarity of the detection of the faint eastern arcs would be surprising if they were pure emission-line structures.

Because we are interested in the ionization mechanism for the extended gas, we have also examined the spatial distributions of the various emission lines in our long-slit spectra. The results are shown for [O III] λ5007 and [O II] λ3727 in Fig. 3, where it can be seen that, while both the [O III] and the [O II] peak in the same position in the western arc, the [O II] falls off more rapidly to the west of the peak; the [O III] emission is also relatively more prominent to the east of the peak. This is partly because of the knot of line emission north-west of the nucleus, which has a higher ionization state than the western arc. The emission from this component becomes more noticeable in the north-

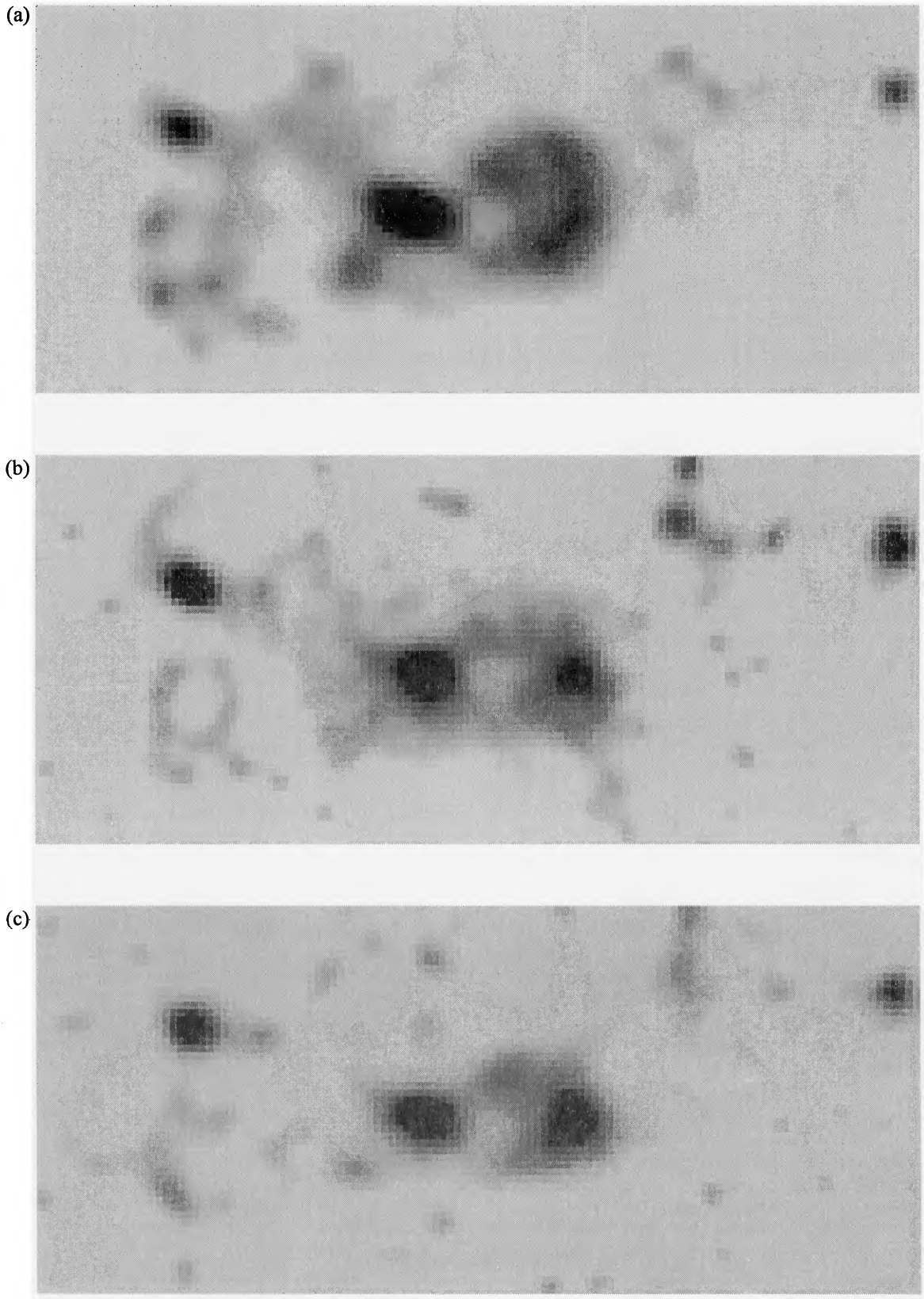

Figure 2. Grey-scale representations of images of PKS 2250 − 41 which have been restored using the Richardson–Lucy algorithm: (a) the narrow-band [O III] image; (b) the broad-band *V* image; (c) the broad-band *B* image. West is to the right, north is to the top, the pixel size is 0.305 arcsec, and all three images cover 37 arcsec east–west and 16 arcsec north–south.

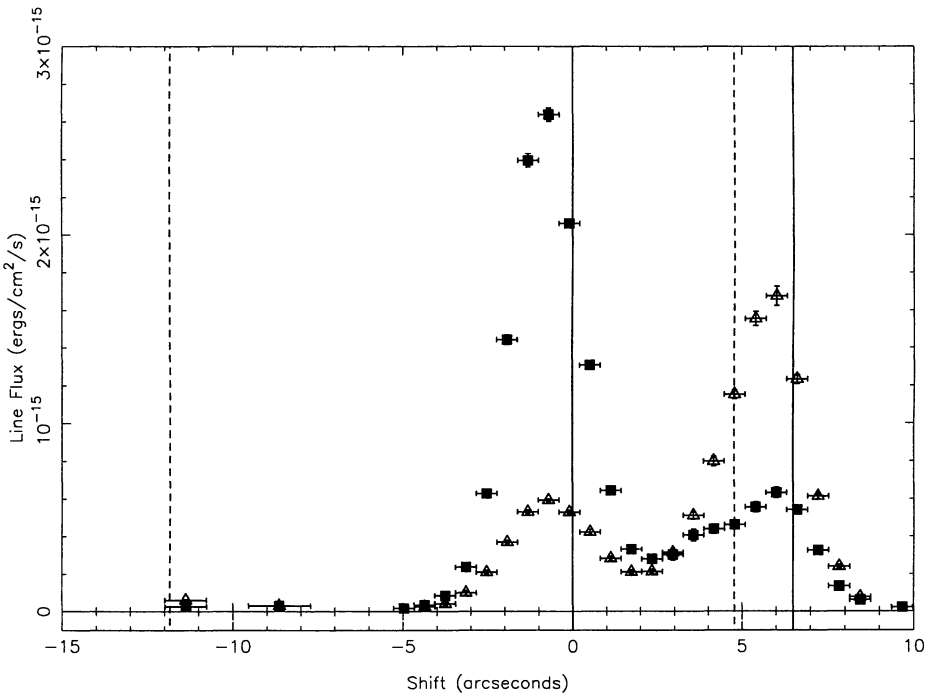

Figure 3. Variation in the strength of the [O III] λ5007 (filled squares) and [O II] λ3727 (hollow triangles) emission lines along the radio axis of PKS 2250 – 41 as measured from the central blue low-dispersion spectrum. In this and subsequent plots, the x axis denotes the displacement from the nuclear nebular-subtracted continuum centroid (west is to the right), the positions of the nuclear and western continuum components are indicated by solid vertical lines, and the centroids of the radio lobes are indicated by dashed lines.

ernmost slit position, which intercepts more flux from the knot.

4.2 The radio data

PKS 2250 – 41 was previously observed at 5 GHz by Duncan & Sproats (1993) and Morganti et al. (1993). Our new total-intensity images are of much higher quality than those previously published, owing to longer observations, improved telescope systems and particularly good phase stability during the night of observation. In addition, we present here a full polarimetric analysis at 5 and 8 GHz, allowing us to investigate the depolarization of this source, which is relevant to the extended optical emission-line gas.

The new 5-GHz images do not provide any significant extra total-intensity information over the higher resolution 8-GHz data, so we present the 5-GHz data only when comparing them directly with the 8-GHz data.

4.2.1 8-GHz total intensity structure

The 5-GHz radio data already available for 2250 – 41 show a source dominated by two bright lobes. These lobes are only slightly resolved at the resolution of those previous observations (typically a few arcseconds).

Our new full-resolution (1.4×1.1 arcsec^2 at position angle 1°.6), 8-GHz radio total-intensity image is shown via a contour map in Fig. 4(a). The rms noise is ~ 0.19 mJy, which gives an excellent dynamic range of more than 1000.

At 8 GHz, the structure of the source is still dominated by two bright and slightly resolved components. In addition, however, low-brightness, extended structure reaching back towards the optical nucleus is now evident. This type of 'bridging' structure is common in FRII radio sources, and is generally thought to be material flowing back from the working surface of the (unseen) radio jet as it interacts with the IGM (Blandford & Rees 1974).

The two lobes are situated asymmetrically compared to the centre of the optical nucleus. The western lobe is at a distance of 4.9 arcsec (~ 28 kpc) from the V-band nucleus of the galaxy, whilst the eastern lobe is 11.9 arcsec (~ 72 kpc) from the nucleus. Despite the high frequency of these observations, no radio core was detected. We find a 3σ upper limit to the core flux density of $S_{\rm core}^{8\,\rm GHz} < 0.8$ mJy (measured at the position of the optical core), and a limit to the core-to-extended flux ratio $R = S_{\rm core}/S_{\rm ext} < 0.013$. The flux densities of the two lobes are listed in Table 3(a).

4.2.2 8-GHz polarized intensity structure

Images of the Stokes parameters Q and U have also been produced, and from these we obtain the polarized intensity image [$(P = (Q^2 + U^2)^{1/2}$] and position-angle image [$\chi = 0.5 \arctan(U/Q)$]. The rms noise of signal-free portion of the Q and U images is $\sigma_{QU} \sim 0.16$ mJy, indicating that the total intensity image is close to its maximum theoretical dynamic range. The polarized intensity and, as a consequence, the fractional polarization ($m = P/I$) were estimated only for the pixels for which $P > 5\sigma_{QU}$. Note that because of this conservative cut-off, the Ricean bias in the P

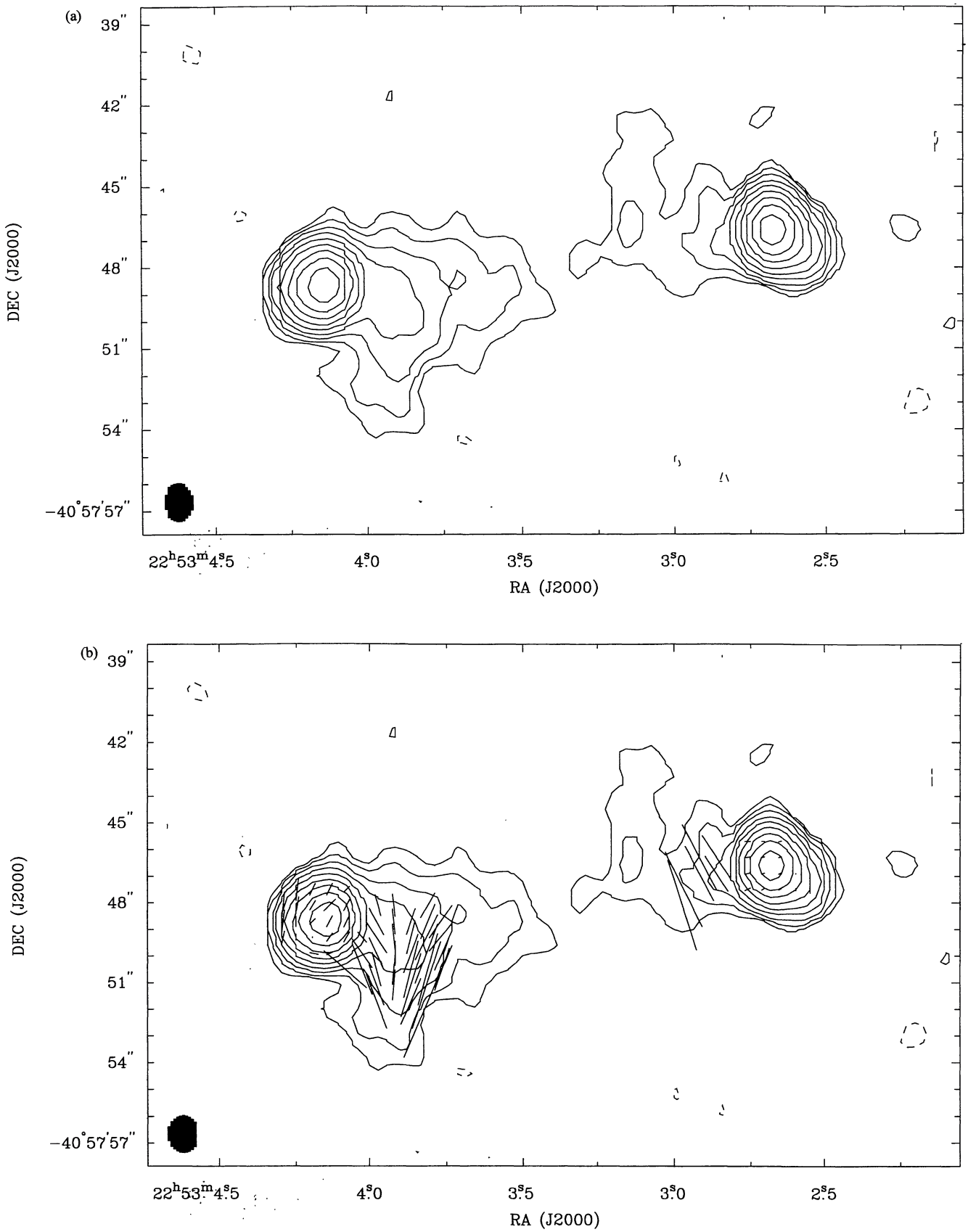

Figure 4. (a) Contour plot of the total intensity at 8 GHz; (b) vectors showing the polarized 8-GHz emission superimposed on a contour plot of the 8-GHz total intensity. The right ascension and declination are J2000 coordinates. The contour levels are $0.85 \times (-1, 1, 2, 4, 8, 16, 32, 64, 128, 256)$ mJy beam^{-1}.

Table 3(a). The observed absolute intensity, polarized intensity and percentage polarization at 8.6-GHz for the western lobe, the eastern lobe and the low surface brightness region of the eastern lobe.

Region	I(mJy)	P(mJy)	m(%)
Lobe W	290.6	7.5	2.6±0.4
Lobe E(all)	382.7	31.2	8.1±0.3
E low bright.	44.9	7.1	15.7 ±2.1

Table 3(b). The observed absolute intensity, polarized intensity and percentage polarization for the two radio lobes at 5.8 and 8.6 GHz, together with the computed spectral index and depolarization ratio. Note that the 8.6-GHz intensity and polarized intensity values differ from those in Table 3(a) because the full-resolution 8.6-GHz images have been degraded to the resolution of the 5.6-GHz images.

Region	I_5(mJy)	P_5(mJy)	m_5(%)	I_8(mJy)	P_8(mJy)	m_8(%)	α_8^5	D_8^5
Lobe W	419.5	3.2	0.8±0.3	267.1	6.1	2.3±0.4	1.18±0.03	0.35±0.09
Lobe E	567.7	38.4	6.8±0.3	380.4	26.3	6.9±0.3	1.04±0.03	0.99±0.04

images is negligible, although a first-order correction was made.

The errors in the fractional polarization have been estimated according to the statistical propagation of errors plus the error in determining the instrumental polarization of the antennae (~ 0.2 per cent) which can be estimated by examining the Stokes V (circular polarization) images (they should be pure noise).

In Table 3(a) we summarize the basic 8-GHz total and polarized intensity quantities in this source. In Fig. 4(b) we show contours of total intensity, plus vectors whose length is proportional to the fractional polarization and whose position angle is that of the nominal projected magnetic field. The electric vector position angle is obtained by adding 90°, assuming negligible Faraday rotation (the maximum rotation measure in the source is ~ 100 rad m^{-2} in the western lobe, which implies a rotation of only 5° at 8 GHz).

The percentage polarization in the western lobe is very low, $m \approx 2.6 \pm 0.2$ per cent, despite the high frequency of the observation, where depolarization effects should be small. In the eastern lobe, the percentage polarization is higher, with values of $m \approx 10 \pm 0.2$ per cent in the hotspot and $m \approx 16 \pm 0.3$ per cent in the extended low-brightness region. Additionally, the sharp outer edge of the eastern lobe shows a small rise in fractional polarization compared with the more central locations in the hotspot. This is again unlike the western lobe, where the sharp outer edge is unpolarized. This rise in m towards the edge may be a result of compressional alignment of the magnetic field caused by the bow shock at the working surface of the jet.

4.2.3 *Comparison with the 5-GHz data*

To compare the 8-GHz data with the 5-GHz data, we have generated 8- and 5-GHz Stokes I, Q and U images at the best 5-GHz resolution (1.94×1.51 arcsec^2 at position angle $-0\overset{\circ}{.}2$). This was done by convolving the 8-GHz visibilities with the appropriate Gaussian during imaging, thus weighting down the longer spacings. All images referred to in this section are at this lower resolution.

Fig. 5(a) shows the 5-GHz total intensity contours with fractional polarization vectors (with the same 5σ cut-off as the full-resolution, 8-GHz data) at the position angle of the nominal projected magnetic field. The western lobe again shows little polarized emission, whilst in the eastern lobe the polarization morphology strongly resembles that of the higher resolution 8-GHz data presented above. To quantify the relative amounts of polarized emission at the two frequencies, we examined the depolarization ratio defined as $D = m_{5\,\mathrm{GHz}}/m_{8\,\mathrm{GHz}}$. Fig. 5(b) shows this quantity superposed on the 5-GHz total-intensity contours. Because the 5σ cut-off used to make the polarized intensity images is conservative, the largest error in the tertiary depolarization ratio image that we encounter is 0.2 (at the edge of the low-surface-brightness extension to the eastern lobe). Elsewhere, because we have very high signal-to-noise ratio polarimetry (maximum $P/\sigma_{Q,U} \approx 150$), the errors are much smaller (see below).

We see that the depolarization in the western lobe is very strong; that is, D is substantially less than unity, and typically we see $D \approx 0.4 \pm 0.05$. On the other hand, the results in the eastern lobe are consistent with no depolarization between 5 and 8 GHz, as $D \approx 1 \pm 0.02$ (see Table 3b).

What is the cause of this depolarization? To investigate this further, we have computed the rotation measure (RM) between 5 and 8 GHz. This is shown in Fig. 5(c). Because we have only two frequencies, we are not able to determine if $N\pi$ ambiguities are present, and the RM presented is the minimum value possible from the data. We find that the RM is $\approx 0 \pm 8$ rad m^{-2} in the brightest part of the eastern lobe, whereas it is RM$\sim +100 \pm 50$ rad m^{-2} in the western lobe, although there are some substantial gradients. In the extended low-brightness region of the eastern lobe, there is an apparent rotation measure gradient from RM ≈ 50 rad m^{-2} at the western edge of the 'bridging' emission to RM ≈ 0 rad m^{-2} in the middle of the hotspot. However, the errors in the RM in the bridging emission are of the order of the values themselves, so the significance of this RM gradient is questionable.

The typical Galactic contribution to the value of the RM in the general direction of 2250 − 41, which is at Galactic coordinates of approximately $(l, b) = (360°, -60°)$, is less than $+30$ rad m^{-2} (Simard-Normandin & Kronberg 1980). This, together with the low RM in the eastern lobe suggests that the additional RM component in the western lobe is local to 2250 − 41.

Depolarization can be attributed to beam smearing or internal Faraday depth effects. The former is almost invariably the cause. In this case, an unresolved RM fluctuation (caused by a Faraday screen anywhere along the line of sight) across the synthesized beam causes the electric vector position angles to rotate (Faraday rotation) across the beam. The vector sum of these vectors taken across the beam gives a reduced amplitude compared with any individual vector. The effect is greater at lower frequencies as the position angles change with the square of the wavelength.

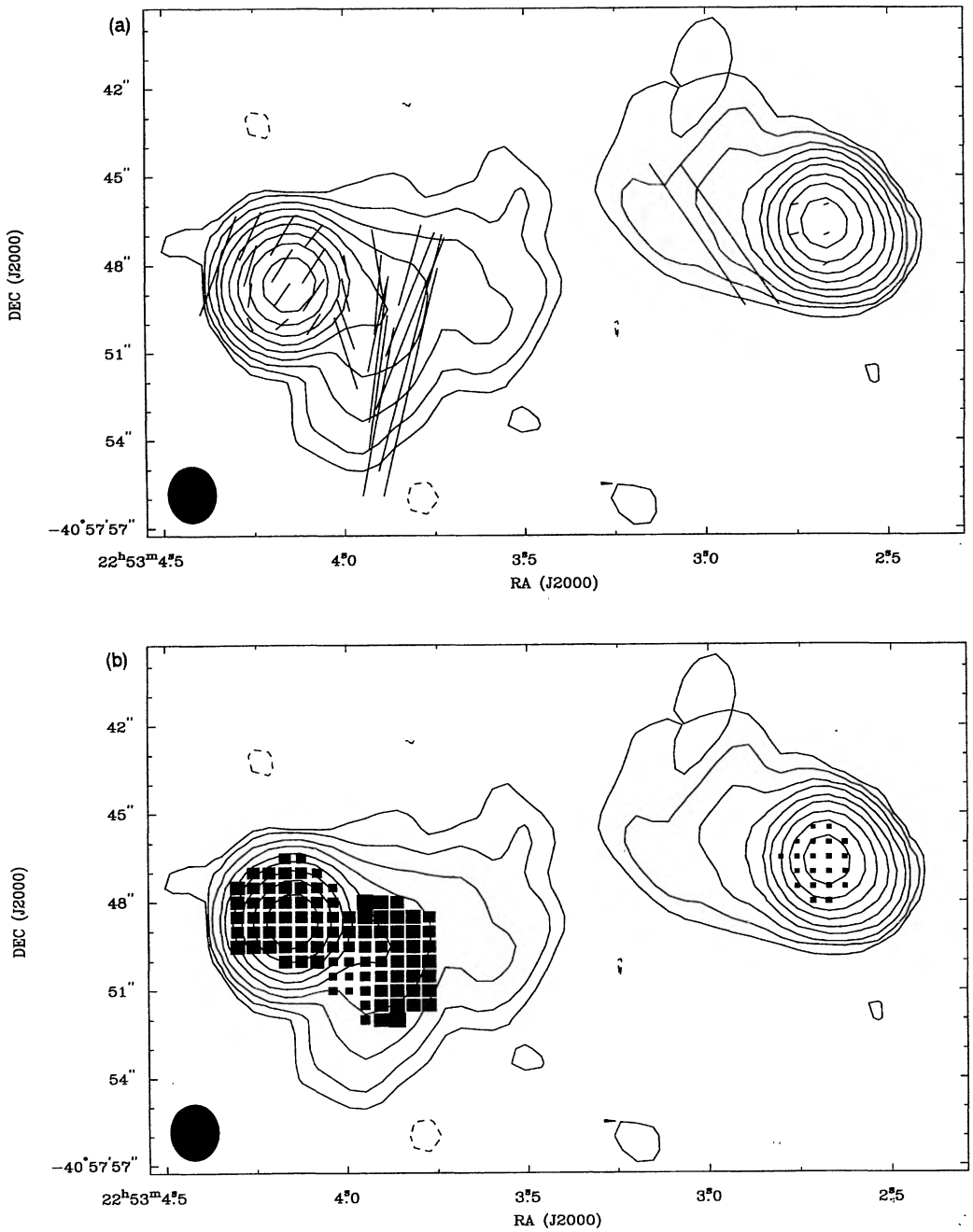

Figure 5. (a) Vectors indicating the fractional polarization at 5 GHz. (b) The depolarization ratio (range plotted from 0.3 to 1.28). (c) The rotation measure (range plotted from −73 to 220). (d) The spectral index (range plotted from 0.25 to 3). In figures (b)–(d) the measurements were made between 5 and 8 GHz; the size of the squares plotted in the figures is proportional to the measured value (hollow squares represent negative values). All measurements are superimposed on a contour plot of the total intensity at 5 GHz.

We can estimate the required gradient needed to cause the observed depolarization from the expression

$$D = \exp\left[-\frac{g_{\rm RM}^2 \Phi^2}{2 \ln 2} (\lambda_1^4 - \lambda_2^4) \right],$$

where Φ is the synthesized beam FWHM in arcsec, $g_{\rm RM}$ is the RM gradient in rad m^{-2} arcsec^{-1}, and λ_1 and λ_2 are the wavelengths in m. From this we find that an RM gradient of some 250 rad m^{-2} arcsec^{-1} is required to cause the depolarization ratio to fall to values of $D \approx 0.4$ as measured in the western lobe. From our *measured* RM image, there are gradients of the order of 100 rad m^{-2} arcsec^{-1} in the western lobe. However, this is only indicative, as one really needs significantly higher resolution observations to measure the, as yet, unresolved RM gradients. Another possibility is that our rotation measures are an underestimate because of $N\pi$ ambiguities. The addition of one turn would easily account for the depolarization, although it is more likely to be excessive. The physical parameters of the line-emitting gas

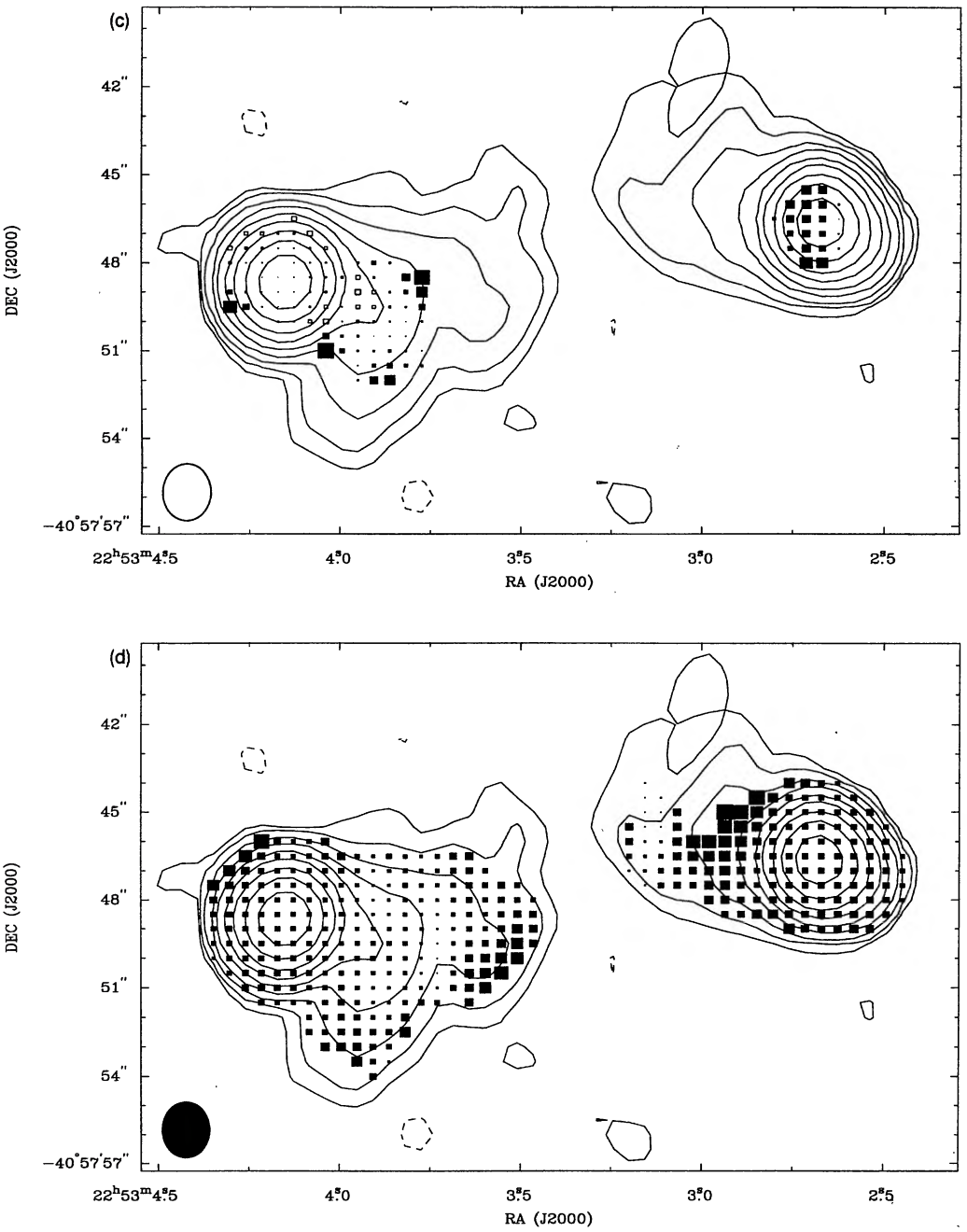

Figure 5 – *continued*

derived from the long-slit spectra (Section 4.3.2) suggest that depolarization by the observed thermal gas is also a possibility; however, pending a four-frequency study of this source, we cannot say more at this time.

Finally, we also computed an image of the spectral index, α (defined as $S_\nu \propto \nu^{-\alpha}$), between 5 and 8 GHz. The results shown in Fig. 5(d) reveal a modest gradient in the spectral index across the source, with typical values of 1.18 ± 0.03 and 1.03 ± 0.03 in the western and eastern lobes respectively (see Table 3b). These values are consistent with the spectral index found with previous single-dish measurements (Kuhr et al. 1981).

We can derive information about the physical conditions in the source assuming equipartition between the energy in magnetic fields and particles (Pacholczyk 1970). If we also assume spherical symmetry, that the ratio (k_p) of energy in other particles to relativistic electrons is unity, that the magnetic-field filling factor is unity, and a spectral index of $+1$ in the frequency range 10 to 10^5 MHz, we can estimate the equipartition field strength, the equipartition pressure and the equipartition energy in the lobes. The values found are summarized in Table 4. However, the many assumptions that go into such calculations render them less than reliable – in particular, the value of k_p is virtually unknown, and is

Table 4. Minimum-energy physical parameters – energy density, B-field, pressure and total energy – for the two radio lobes.

Region	Energy Density	B-Field Strength	Pressure	$\mathrm{Log_{10}}$(Total Energy)
	10^{-10} ergs cm^{-3}	10^{-5} Gauss	10^{-10} dynes cm^{-2}	ergs
Lobe W	5.27	7.51	2.80	59.20
Lobe E	2.13	4.72	1.14	59.70

assumed to be unity largely for convenience (it is several hundred in our Solar system).

4.2.4 *Comparison between the radio and optical data*

The high resolution of the 8-GHz observations allows us to make accurate measurements of the positions of the radio lobes. The positions (J2000) of the lobes from the new data are listed with the positions of the optical components measured from the V-band image in Table 5. The positions of the optical components were obtained by making fits to bright stars on the UK Schmidt plate J8022c, using the automatic plate-measuring facility at the Institute of Astronomy, Cambridge. An astrometric solution was derived using a standard six-coefficient plate model. The main source of error in the positions is the systematic error arising from differences in the radio and optical astrometric reference frames: the rms uncertainty for the optical positions is ≤ 0.2 arcsec internally, but ~ 0.5 arcsec with respect to an external reference frame (R. McMahon, private communication).

Table 5. Radio and optical astrometry. The centroids of the radio components were calculated at 8 GHz; the centroids of the optical components were calculated from the V-band image.

Component	R.A. (error)	Dec. (error)
W Radio Lobe	22:53:02.680 (0.003)	-40:57:46.49 (0.03)
E Radio Lobe	22:53:04.148 (0.005)	-40:57:48.50 (0.03)
Optical Nucleus	22:53:03.11 (0.02)	-40:57:47.17 (0.2)
Western Arc	22:53:02.57 (0.02)	-40:57:47.24 (0.2)

In Fig. 6, we overlay the [O III] emission-line image and the 8-GHz, total-intensity contours. Clearly, the optical and radio emission are closely associated. The western arc of line emission is at the outer edge of the western radio lobe, and the lower surface-brightness eastern arc lies at the inner edge of the eastern radio lobe. Optical continuum emission is also seen coincident with the western lobe and at the inner edge of the eastern lobe. As discussed above, there is a

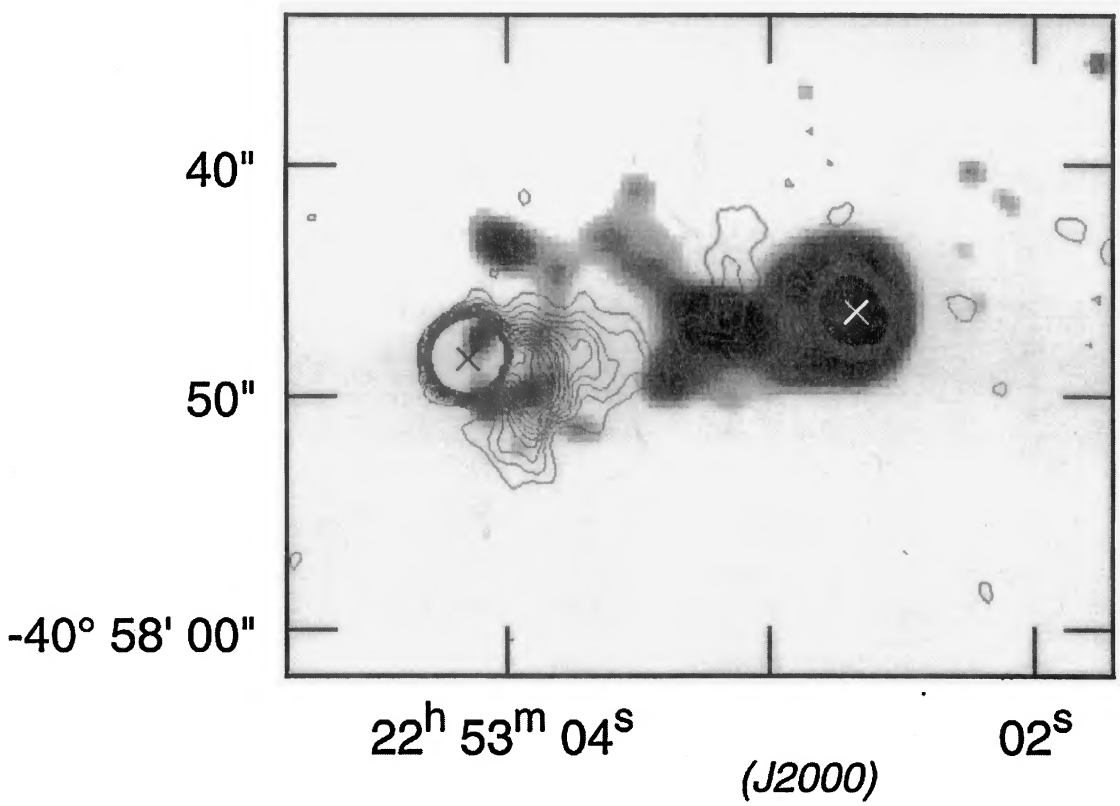

Figure 6. Grey-scale representation of the restored narrow-band [O III] image of PKS 2250 – 41 with contours of the 8-GHz total intensity radio map overlaid. The positions of the radio lobe centroids are indicated by crosses.

possible systematic error in the relative positions of the radio and optical components, but the size of the uncertainty is not large enough to affect the result that *the line and continuum emission in the western arc peak significantly beyond the centre of the radio lobe:* the peaks of the line emission and nebular-subtracted continuum emission (see Section 4.3.4) in the western arc are displaced by 1.3 ± 0.5 arcsec (7.8 ± 3.0 kpc) and 1.5 ± 0.5 arcsec (9.0 ± 3.0 kpc) to the west of the radio lobe respectively.

From comparisons between Figs 5(b) and 6 it is also clear that the line emission and the radio polarization are anti-correlated, particularly in the western lobe, where the arc of [O III] emission circumscribes the polarized radio emission. This strongly suggests that the emission-line gas is responsible for the excess RM in the western lobe and also its strong depolarization. In particular, the sharp outer edge of the western lobe, where the arc of emission-line gas sits, is completely depolarized, whereas the same region of the eastern lobe, where there is no emission-line gas, shows increased fractional polarization. A multifrequency study of the polarimetric characteristics of the source (currently under way) will enable us to determine whether the line-emitting gas is mixed in with the radio plasma or external to it.

The asymmetries that we find in the radio and optical data for PKS 2250 − 41 are consistent with those found in past studies of radio galaxies. The western radio lobe has a steeper spectral index than the eastern lobe, agreeing with the finding by Liu & Pooley (1991) in a sample of radio galaxies that the radio lobe closest to the nucleus generally has the steepest spectral index. Liu & Pooley also found that the greatest depolarization usually occurs in the lobe nearest the centre and in the lobe with the steeper spectral index, which again agrees with the PKS 2250 − 41 data. Our data also support the observation by McCarthy et al. (1990) that the extended emission-line gas around radio galaxies is found preferentially on the side with the shortest radio-lobe length from the nucleus.

4.3 Optical spectroscopy

In this section we present the results derived from our long-slit spectra. The formal errors in the calculated line fluxes from the Gaussian fits to the lines are of the order of a few per cent for the strong lines, rising to up to $\approx \pm 15$ per cent for weaker or blended lines. However, there are also uncertainties inherent in the flux-calibration process, and we estimate systematic errors of $\approx \pm 10$ per cent in the calculated line-flux ratios caused by the relative flux calibration. The red AAT and blue ESO spectra of the integrated nuclear emission and the extended emission are displayed in Figs 7 and 8.

4.3.1 The spectra of the western arc and the nuclear region

Tables 6 and 7 give a full list of the line strengths (relative to the observed Hβ flux) in the western arc and the nucleus for the blue and red long-slit spectra respectively. Since the relative strengths of the Balmer lines are consistent with case B recombination values within the errors (see Osterbrock 1989), no reddening correction has been applied.

It is clear that the western arc has a much lower ionization state than the nucleus. This is graphically illustrated in Fig. 9, which shows the variation in several important diagnostic line ratios along the slit. Although there are differences in detail, all the line ratios show a similar trend, with a pronounced minimum in the ionization state of the extended gas close the peak of the continuum emission in the western arc. This reinforces the earlier result of Tadhunter et al. (1994), which was based on the [O II]3727/[OIII]5007 ratio.

As well as significant ionization structure in the *radial* direction, we also find evidence for structure in the *tangential* (north–south) direction. Fig. 10 shows the variation in the [O II]3727/[O III]5007 line ratio for the three blue EFOSC spectra. A clear ionization minimum is found at the position of the western arc in all three slit positions, but the ionization state is lowest in the central slit position. Although similar trends are noted on the eastern side of the nucleus, there are no obvious tangential ionization gradients in the nuclear regions ($r < 15$ kpc).

4.3.2 Physical conditions

The physical conditions in the EELR provide important clues to the nature of the relationship between the optical and radio-emitting comonents. Our data are of sufficient quality to allow us to measure the electron temperature, density and pressure in the bright western arc.

The measured value of the [S II]6717/6731 diagnostic ratio ([S II]6717/6731 $= 1.26 \pm 0.04$) leads to an electron density of $n_e = 170 \pm 50$ cm^{-3} for the western arc. Note that residual CCD fringing is a potential problem for measuring the [S II] $\lambda\lambda$6717, 6731 lines, because it affects the quality of the sky subtraction at near-infrared wavelengths. However, by examining the residuals of night-sky lines along the slit in the wavelength range of interest, we estimate that the uncertainty in the [S II](6717/6731) ratio resulting from the residual fringing is < 3 per cent at the position of the western arc. For the nuclear region, the relative weakness of [S II], coupled with the fringing problems, meant that a reliable measurement of the density was not possible.

The electron temperature for the emission-line gas in the western arc has been estimated using the [O III](4959 + 5007)/4363 diagnostic line ratio, and assuming the low-density limit. The measured value for this ratio of 60 ± 10 leads to $T_e = 15\,000 \pm 2000$ K for the western arc. This is typical of the temperatures found in the EELR of radio galaxies in general (Tadhunter, Robinson & Morganti 1989). For the nucleus, estimating the electron temperature is complicated by the significant structure in the stellar continuum underlying the weak [O III] λ4363 feature. Following the subtraction of the best-fitting power-law + elliptical-galaxy continuum model (R. Dickson, private communication), we measure [O III](4959 + 5007)/4363 $= 96 \pm 8$, indicating an electron temperature of $T_e = 13\,000 \pm 700$ K.

By combining the calculated electron temperature and density for the western arc, we derive a pressure for the warm gas in the western arc of $P_e \sim 2n_e kT = 7 \times 10^{-10}$ dyn cm^{-2}. Note that this pressure is orders of magnitude higher than measured in the hot X-ray haloes of groups of galaxies of comparable X-ray luminosity. For example,

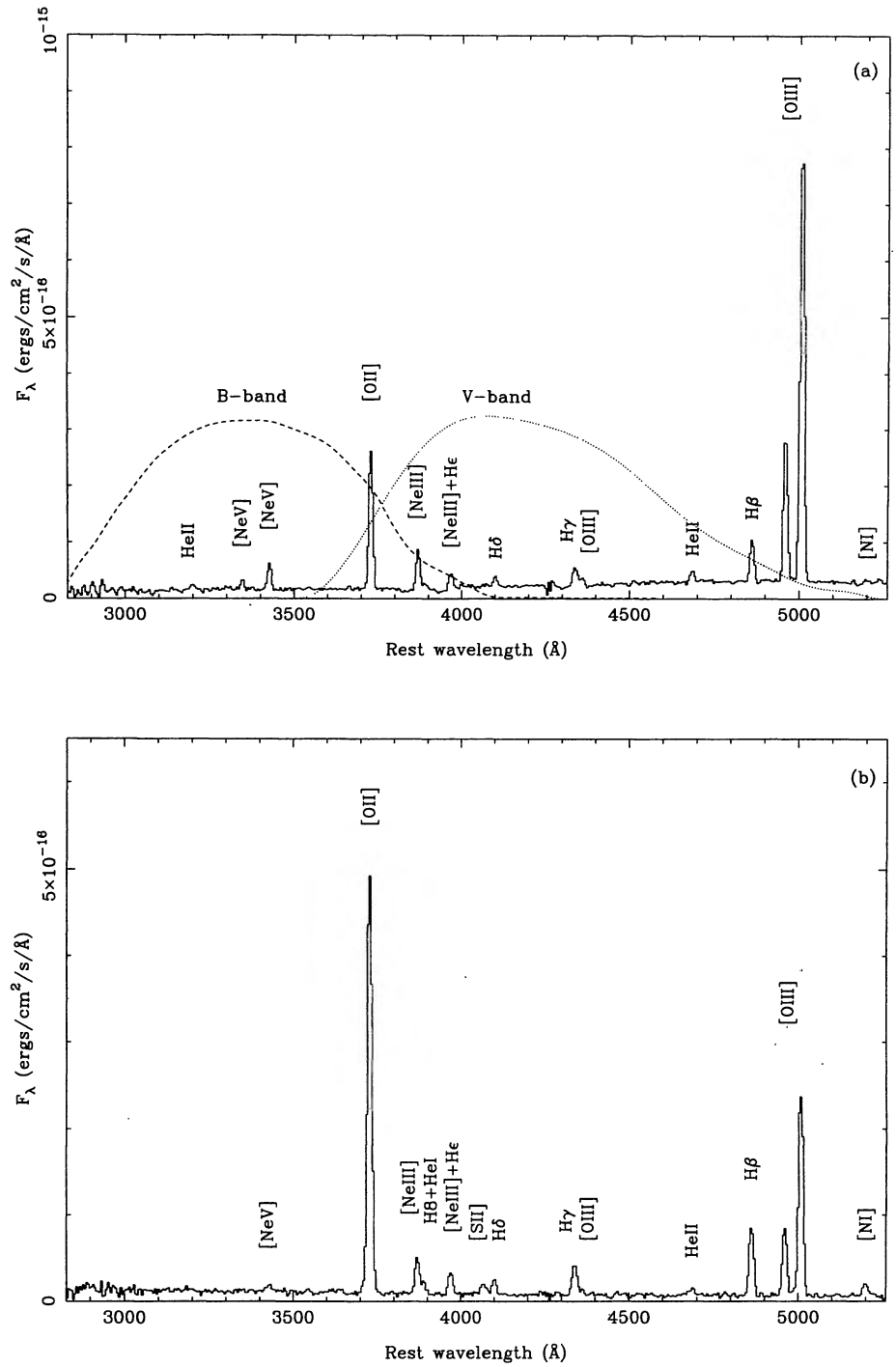

Figure 7. Spectra of PKS 2250 – 41 extracted from the central blue long-slit spectrum: (a) the nuclear region (within a 3.0-arcsec radius of the nuclear continuum centroid); (b) the western arc (within a 3.0-arcsec radius aperture centred 6.0 arcsec west of the nucleus). The response functions for the broad-band *B* and *V* filters are overlaid on the nuclear spectrum.

using the data in Ponman et al. (1994), we estimate that the X-ray halo around the candidate fossil galaxy group RXJ 1340.6 + 4018 has a pressure of only $\sim 6\times10^{-12}$ dyn cm^{-2} at a radius of 40 kpc from the nucleus. On the other hand, the pressures in the warm emission-line clouds are entirely consistent with the minimum pressures in the radio lobes as estimated from the radio observations (Table 4).

We can also estimate the mass of ionized warm gas and the filling factor. Following Osterbrock (1989), the Hβ luminosity $L_{H\beta}$ for a pure hydrogen nebula is given by

$$L_{H\beta} = h\nu_{H\beta} V \varepsilon n_e n_p \alpha^{\rm eff}_{H\beta},$$

where h is Planck's constant, $\nu_{H\beta}$ is the frequency of the Hβ line, V is the volume of the emitting region, n_e and n_p are the electron and proton densities, and $\alpha^{\rm eff}_{H\beta}$ is the effective

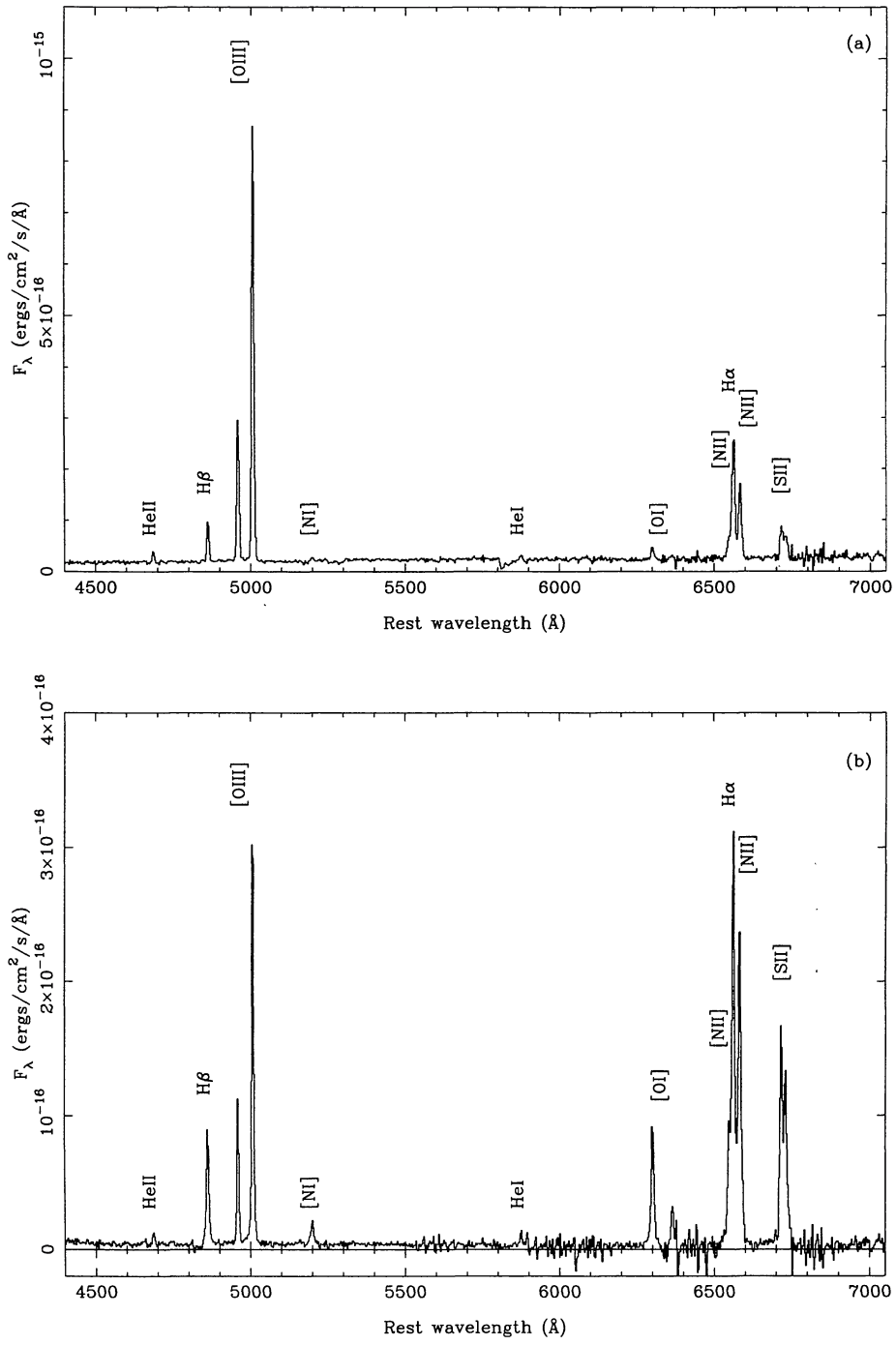

Figure 8. Red spectra of PKS 2250 – 41: (a) the nuclear region (within a 3.2-arcsec radius of the nuclear continuum centroid); (b) the western arc (within a 3.2-arcsec-radius aperture centred 6.0 arcsec west of the nucleus).

recombination coefficient. Assuming cylindrical symmetry for the western arc, this gives an estimate for the volume filling factor for case B recombination of $\varepsilon \sim 5 \times 10^{-8}$ – lower than is generally found in the EELR of radio galaxies ($\varepsilon \approx 10^{-5}$; see, e.g., Morganti et al. 1991). This could indicate that the assumed geometry is incorrect; for example, the emission gas could be distributed in a thin shell, rather than a filled cylinder. Thus the estimated filling factor is likely to be a lower limit.

The mass of line-emitting gas in the EELR can be estimated in a similar way; from simple recombination theory,

$$M = \frac{L_{\mathrm{H}\beta} m_{\mathrm{H}} \mu}{n_{\mathrm{e}} \alpha^{\mathrm{eff}}_{\mathrm{H}\beta} h \nu_{\mathrm{H}\beta}},$$

where m_{H} is the mass of atomic hydrogen, and μ is the mean atomic mass. This leads to an ionized gas mass of $M \sim 2 \times 10^6\,\mathrm{M}_\odot$ for the western arc. However, given that

Table 6. The emission-line fluxes for the nuclear region (central slit position), and the western arc (all three slit positions) as derived from the blue long-slit spectra (same aperture for both regions).

			Western Arc		
Wavelength(Å)	Line	Nucleus	Central	South	North
3343	[NeV]	0.25	–	–	–
3424	[NeV]	0.67	0.13	0.06	–
3727	[OII]	3.20	5.53	6.82	6.30
3865	[NeIII]	0.89	0.48	0.54	0.65
3886	H8+HeI	–	0.16	–	0.14
3967	[NeIII]+Hϵ	0.40	0.30	0.34	–
4071	[SII]	–	0.16	0.20	0.14
4102	Hδ	0.26	0.18	0.23	0.27
4340	Hγ	0.44	0.43	0.46	0.46
4363	[OIII]	0.18	0.07	0.06	–
4686	HeII	0.27	0.14	0.11	–
4861	Hβ	1.00	1.00	1.00	1.00
4959	[OIII]	3.74	1.00	0.95	1.40
5007	[OIII]	11.18	2.96	3.02	4.13
5199	[NI]	0.07	0.21	0.18	0.20
$F_{H\beta}(10^{-16}$ ergs s^{-1} cm$^{-2})$		6.4	9.4	6.4	5.4

Aperture: 2.0 × 6.1 **arcsec**

neutral and/or molecular gas may be present (but not yet observed), this is a lower limit on the *total* gas mass.

4.3.3 *Emission-line kinematics*

The emission-line kinematics derived from the long-slit spectra provide information about the origins of the extended gas and the possible disturbing influence of the radio jets.

Surprisingly, given the morphological evidence for a jet/cloud interaction, the radial velocity amplitudes are small (see Fig. 11a): from the higher dispersion red spectra we measure a maximum rest-frame radial velocity amplitude of only $\Delta V_{\rm tot} < 200$ km s^{-1} – at the lower end of the range measured for EELR in low-redshift radio galaxies (Tadhunter et al. 1989a). This implies that, if the emission-line gas is undergoing high-velocity systematic motions, then these motions must be confined to the direction perpendicular to the line of sight (i.e., the sky plane).

Although there is no sign of extreme non-gravitational motions in the radial velocity variations, there is strong evidence for kinematic disturbance from the linewidth measurements. Fig. 11(b) shows the spatial variations in the widths of various emission lines across the nebulosity, while Table 8 lists the linewidths measured from the spatially integrated red spectrum of the western arc. Some clear trends emerge: the low-ionization lines – [N II], [S II] and [O I] – are relatively broad across the entire nebulosity, with spatially integrated linewidths in the western arc of 410–480 km s^{-1} (FWHM). In contrast, the high-ionization

Table 7. The emission-line fluxes for nuclear and western arc as derived from red long-slit spectrum (same aperture for both regions).

Wavelength(Å)	Line	Nucleus	Western Arc
4686	HeII	0.28	0.10
4861	Hβ	1.00	1.00
4959	[OIII]	3.86	0.97
5007	[OIII]	11.74	3.02
5199	[NI]	0.13	0.26
5875	HeI	0.15	0.10
6300	[OI]	0.43	1.30
6363	[OI]	–	0.43
6548	[NII]	0.74	1.49
6563	Hα	4.33	4.08
6584	[NII]	2.39	3.48
6717	[SII]	1.33	2.32
6731	[SII]	0.76	1.79
$F_{H\beta}(10^{-16}$ ergs s^{-1} cm$^{-2})$		5.8	7.6

Aperture: 1.5 × 6.5 **arcsec**

[O III] lines are significantly narrower throughout the western arc, with an integrated linewidth of 240 ± 10 km s^{-1}. The Balmer lines have intermediate linewidths (FWHM ~ 400 km s^{-1}). To our knowledge, such kinematic differentiation of the low- and high-ionization lines is without precedent in the published studies of EELR in radio galaxies; the behaviour is the reverse of that observed in the nuclear narrow-line regions (NLR) of Seyfert galaxies, where it is the higher ionization lines that tend to be the broader (e.g. de Robertis & Osterbrock 1984).

We emphasize that the observed variation of linewidth with ionization state cannot be the result of instrumental effects. Measurements of the widths of a number of arc and night-sky lines show no systematic variation with wavelength in the long-slit spectra. Also, the fact that (a) all of the emission lines have similar widths in the nucleus, and (b) the observed widths of the Hα and Hβ lines – which are at opposite ends of the red spectra – agree well, demonstrates that the linewidth measurements are reliable. The dependence of linewidth on ionization state can be seen directly by comparing the profiles of Hβ with [O III] λ4959 in Fig. 12.

Along with the observed anticorrelation between linewidth and ionization state we find a gradual decrease in linewidth towards the outer edge of the western arc. This can be seen particularly clearly in the [O III] lines, but is also apparent in the lower ionization lines beyond a radius of about 5 arcsec (30 kpc). The stronger lines are also resolved in the eastern arcs, and these linewidths are also plotted in Fig. 11(b).

All the results presented so far have been for the strong cores of the emission lines which dominate the linewidth measurements. However, even at the relatively low resolution of our observations, we begin to see some faint kinematic substructure. A particularly notable feature is the very extended blue wings to the [O III] lines which are visible in

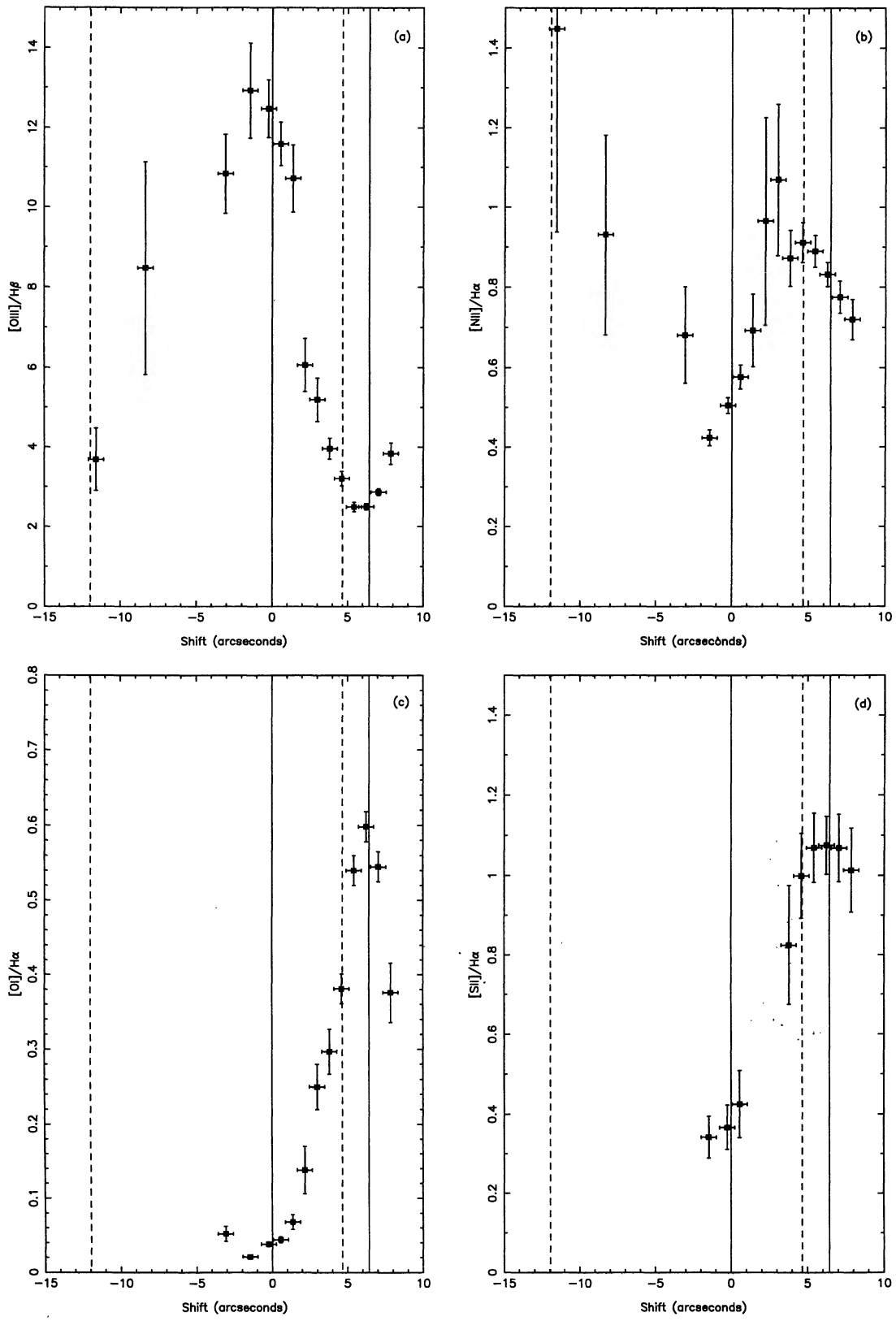

Figure 9. Variation in several important line ratios along the radio axis of PKS 2250 – 41, from the red long-slit spectrum: (a) [O III] λ5007/Hβ; (b) [N II] λ6584/Hα; (c) [O I] λ6300/Hα; (d) [S II] (6717 + 6731)/Hα.

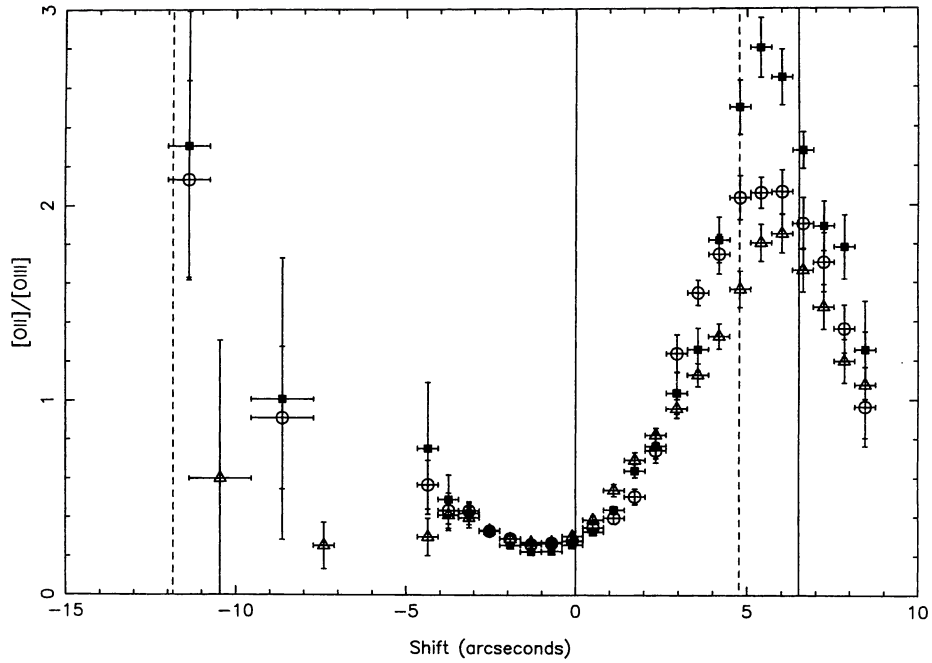

Figure 10. Variation in the [O II] λ3727/[O III] λ5007 line ratio along the radio axis from the northernmost (hollow triangles), central (filled squares) and southernmost (hollow circles) blue long-slit spectra.

the red spectra of the western arc but not in the red spectrum of the nucleus. The wings are best seen in the [O III] λ5007 line, where they extend over 30 Å (see Fig. 12). Similar blue wings have been observed in the EELR of the low-redshift radio galaxy PKS 2152 − 69 (Tadhunter et al. 1988a) and in the core region of Cygnus A (Tadhunter 1991). The wings may also be present in the lower ionization lines of PKS 2250 − 451, but the signal-to-noise ratio of our spectra is not high enough to detect them.

4.3.4 Broad-band continuum magnitudes

Dickson et al. (1995) have noted much of the UV excess in the continuum spectrum of the western arc is caused by the nebular continuum emitted by the warm emission-line clouds. This is illustrated by Fig. 13, which shows the spatial profile of the UV continuum before and after the nebular continuum component estimated from the spatial profile of the UV continuum before and after the nebular continuum component estimated from the spatial profile of Hβ has been subtracted. Following subtraction, the peak of the residual UV continuum becomes displaced to the west of the emission-line peak (by ~ 0.2 arcsec).

To gain clues to the origin of the residual, nebular-subtracted, continuum emission, we have calculated rest-frame optical magnitudes and colours for the different continuum-emitting components (the nuclear region, the western arc and the neighbouring galaxy). This has been done by measuring the continuum fluxes in the wavelength ranges close to the effective wavelengths of the standard B, V and R broad-band filters, taking care not to include strong emission lines. The results are presented in Table 9. Note that these magnitudes can be regarded as lower limits on the continuum brightnesses, since the slit provided only partial coverage of the regions considered. The colour and luminosity of the residual continuum in the western arc are characteristic of late-type spiral or irregular galaxies of moderate luminosity.

4.4 X-ray images

PKS 2250 − 41 is marginally detected at the $\sim 2\sigma$ level in the 0.1 to 2.4 keV band by the *ROSAT* HRI camera: by integrating the counts in the source over a 15.0-arcsec diameter circular aperture, and subtracting the mean background level estimated in an annulus of inner radius 20 arcsec and outer radius 80 arcsec, we estimate that we have detected 10 ± 5 photons from PKS 2250 − 41 in an integration time of 21 028 s. This corresponds to a count rate of $4.8(\pm 2.4) \times 10^{-4}$ photon s^{-1}. Our confidence in the detection is increased by the fact that we also detect the F star HD 216363 in the image, with the correct spatial offset from the assumed position of PKS 2250 − 41.

With no information about the X-ray spectrum of the source, it is necessary to assume a spectral model in order to calculate the X-ray flux and luminosity. Adopting a power-law model and a Galactic neutral-hydrogen column of $N_{\rm H} = 1.42 \times 10^{20}$ cm^{-2}, we find that we obtain a flux of $F = (3.5 \pm 1.7) \times 10^{-14}$ erg cm^{-2} s^{-1} and a luminosity $L = (1.6 \pm 0.8) \times 10^{43}$ erg s^{-1} for a power-law photon index of 1.5, while for a photon index of 3.0 the corresponding figures are $F = (6.1 \pm 3.0) \times 10^{-14}$ erg cm^{-2} s^{-1} and $L = (4.3 \pm 2.1) \times 10^{43}$ erg s^{-1}. Alternatively, a thermal-bremsstrahlung model with a gas temperature $T = 3 \times 10^7$ K gives $F = (3.1 \pm 1.5) \times 10^{-14}$ erg cm^{-2} s^{-1} and $L = (1.7 \pm 0.8) \times 10^{43}$ erg s^{-1}.

To place these estimates in context, the X-ray luminosities are comparable to those measured for the hot X-ray-

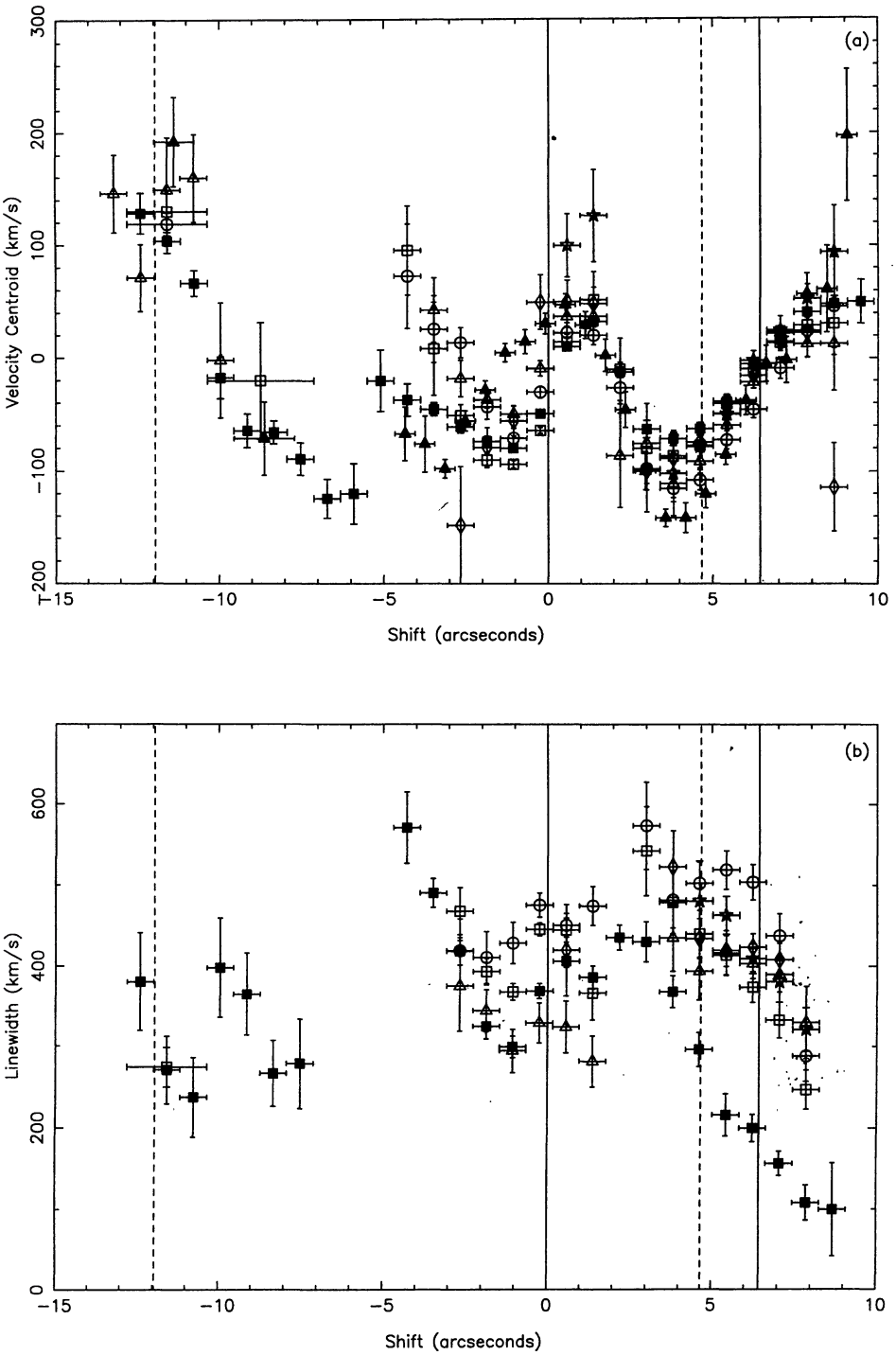

Figure 11. Variation in the (a) radial velocity centroids and (b) linewidths (FWHM) along the radio axis of PKS 2250 – 41 as derived from the red long-slit spectra. The emission lines are identified as follows: [O III] λ5007 (filled squares), Hα (hollow squares), Hβ (hollow triangles), [N II] λ6584 (hollow circles), [O I] λ6300 (hollow diamonds) and [S II] λ6717 (hollow stars). The velocity variation of [O III] λ5007 (filled triangles) measured from the southernmost blue spectrum is also plotted.

emitting as in groups of galaxies (10^{41}–5×10^{43} erg s^{-1}; Ponman et al. 1994), but are significantly lower than those measured for the hot X-ray haloes of rich clusters of galaxies. Whatever the origin of the X-ray emission from PKS 2250 – 41, it is clear that the hot gaseous environment of the source is at best only moderately rich.

5 DISCUSSION

The results presented in the previous sections provide evidence for an intimate relationship between the radio and optical components in PKS 2250 – 41. By way of summarizing the main results, we note the following features.

Table 8. The integrated rest-frame emission-line widths (FWHM) for the western arc derived from the red long-slit spectrum. The widths have been quadratically corrected for the instrumental width.

Wavelength(Å)	Line	Linewidth/km s^{-1}
4686	HeII	390 ± 80
4861	Hβ	430 ± 20
5007	[OIII]	240 ± 10
6300	[OI]	450 ± 30
6563	Hα	400 ± 20
6584	[NII]	480 ± 20
6717	[SII]	410 ± 20

Aperture: 1.5 × 6.5 **arcsec**

Structural associations between the radio and optical emission. The emission-line and continuum features to both the east and the west of the nucleus are situated at the boundaries of the radio lobes; the western radio lobe gives the appearance of being confined and constrained by the external gas. There is also evidence for a gap in faint arcs to the east of the nucleus, which may be the result of the radio jet tunnelling through and disrupting/dispersing the ISM (as may also be the case in Cygnus A; Jackson et al. 1993).

Radio depolarization. The high depolarization observed in the western lobe may be the result of the depolarizing effect of a dense, irregular external medium. This is supported by the fact that the edge of the lobe coincident with the arc of ionized gas is unpolarized even at 8 GHz; the [O III] emission and the polarized radio emission show a direct anticorrelation in the western lobe. The eastern lobe appears to suffer less from the interaction with the environment, which agrees with this explanation of the depolarization, as the line emission is also much weaker.

Ionization minimum in the western radio lobe. The observed minimum in the ionization state of the EELR close to the western radio lobe – as measured from several line ratios – is evidence that the radio plasma has a direct effect on the ionization state of the gas.

Pressure balance. The estimated minimum pressure of the radio plasma in the western radio lobe is consistent with the pressure of the emission-line gas. This suggests that the radio plasma and the line-emitting as are in approximate pressure equilibrium.

Linewidths and ionization state. The observed anticorrelation between linewidth and ionization state, which is observed only in the western arc, provides evidence for a kinematic disturbance associated with the radio lobe.

Having established clear evidence for a jet/ISM interaction in this source, we now go on to consider the physical mechanisms involved.

5.1 Photoionization or jet-induced shocks?

A key issue for powerful radio galaxies in general is the extent to which the emission-line properties are defined by central source illumination, and the extent to which they are defined by jet/cloud interactions. We now address this issue

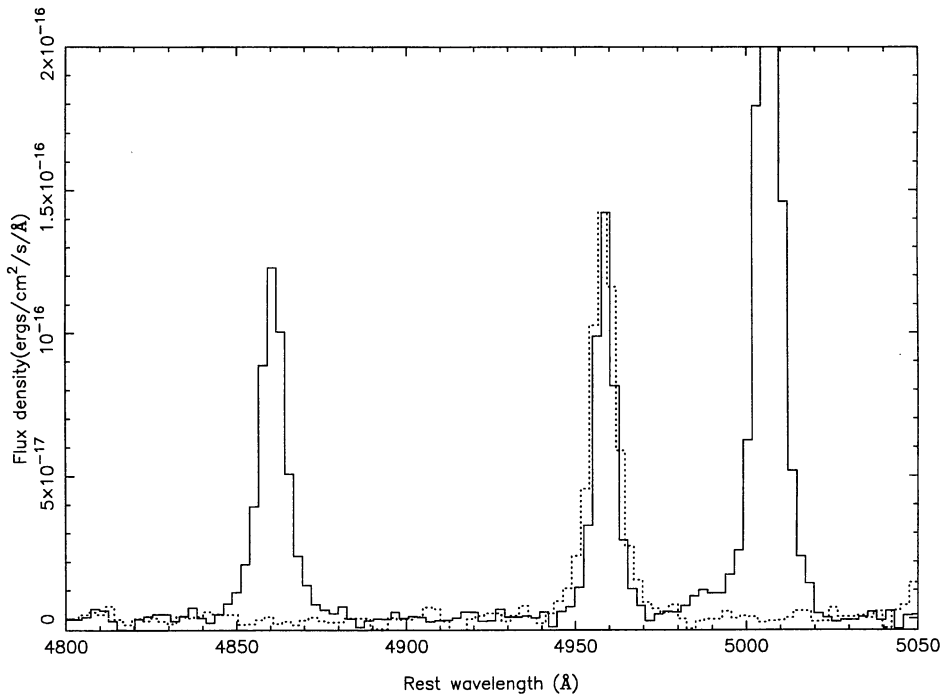

Figure 12. An expanded plot of the [O III] and Hβ line profiles from the red spectrum of the western arc (aperture as for Fig. 8). The dotted line shows the Hβ profile shifted and scaled to the [O III] λ4959 profile, emphasizing the general breadth of Hβ relative to [O III] λ4959. Note also the faint blue wing to the [O III] λ5007 line.

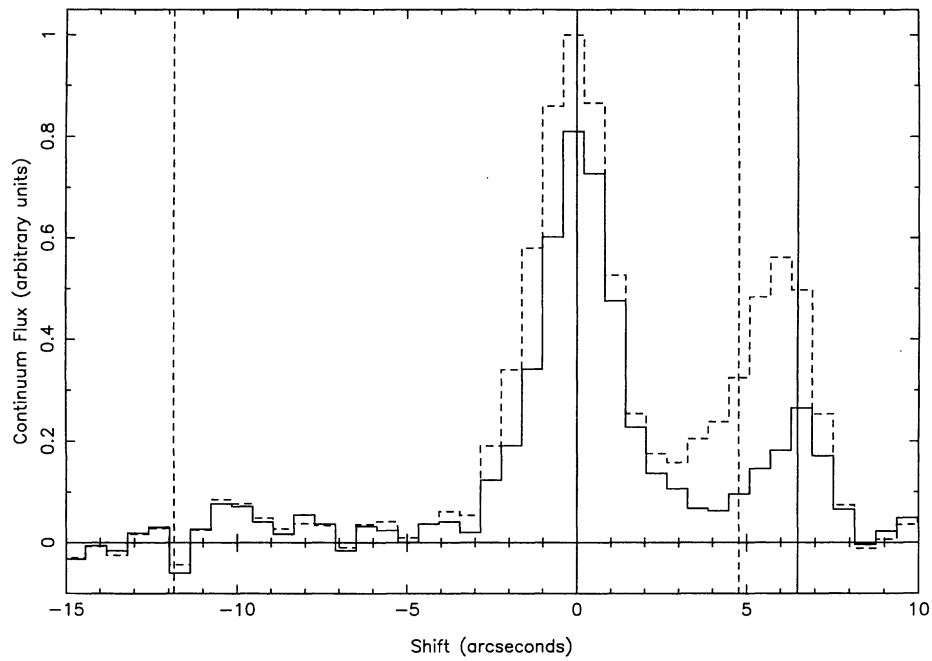

Figure 13. Profile of the near-UV (3460–3680 Å) continuum emission along the radio axis of PKS 2250 – 41 from the central blue long-slit spectrum. The dashed line shows the total continuum profile, while the continuous line shows the nebular-subtracted continuum profile.

Table 9. Photometry of the nuclear region and the western arc. The absolute magnitudes were calculated using a distance modulus $m-M=41.67$. The blue spectrum from the central slit position was used for the extended arc and the nuclear region; the magnitudes for the companion galaxy were calculated from the northernmost blue long-slit spectrum. In all cases an extraction aperture of 3.7×2.0 was used. Note that the colours have been corrected for nebular continuum emission.

Component	m_V	M_V	U-B	B-V	R-V
Nuclear Region	20.7	-21.0	0.1	1.1	1.1
Western Arc	22.3	-19.4	-0.2	0.8	0.6
Companion Galaxy	22.6	-19.1	0.4	0.8	—

for PKS 2250 – 41 by examining the ionization mechanism for the extended gas.

5.1.1 *Photoionization*

We first consider whether our results for PKS 2250 – 41 are consistent with the central source photoionization model which as been so successful in explaining the line ratios in EELR around other radio galaxies (Robinson et al. 1987).

From the plots of the variation in line ratios with position along the slit (Fig. 9) it is clear that there is an ionization minimum close to the centre of the western radio lobe. In terms of central source photoionization this indicates a minimum in the ionization parameter, U, defined by

$$U=q/(cn_e r^2),$$

where q is the total number of ionizing photons emitted per second per unit solid angle by the ionizing source, r is the distance between the nucleus and the EELR, c is the speed of light, and n_e is the electron density. It is clear that, if the EELR are ionized by a central UV source, the observed minimum in the ionization parameter corresponds to a density peak in the extended arc. However, this is difficult to reconcile with AGN illumination of the ambient ISM of the best galaxy, since we expect the density of the ambient medium to be a monotonically decreasing function of radius. One possibility is that, while the gas may be photoionized by a central AGN, the density of the EELR is enhanced by shocks associated with the radio jets (see next section). Alternatively, the density might be relatively high because the gas is gravitationally bound in a companion galaxy, so that the density and pressure in the cloud do not reflect the conditions in the halo of the PKS 2250 – 41 host galaxy, but rather those of the companion. It is notable in this context that the pressure in the warm gas is somewhat greater than would be expected at such a large distance from the nucleus of a relatively isolated early-type galaxy or group of galaxies.

It is also important to consider whether central source illumination is energetically feasible. The above relationship between ionizing luminosity (q) and ionization parameter (U) can be rearranged to give the following expression:

$$q=cn_e Ur^2=cn_e Ud^2\,\mathrm{cosec}^2 i > cn_e Ud^2,$$

where d is the projected radial distance from the nucleus, and i is the inclination of the EELR-nucleus axis to the line of sight. Using the ionization parameter calculated from the [O II]/[O III] ratio for the central slit position ($U=8\times10^{-4}$; Penston et al. 1990), the electron density esti-

mated from the [S II] 6717/6731 ratio, and the projected nucleus–arc distance, we obtain $q > 5 \times 10^{55}$ photon s^{-1} sr^{-1} for the western arc. To place this number in context, a similar calculation for the powerful low-z radio galaxy Cygnus A gives $q \sim 10^{54}$ photon s^{-1} sr^{-1}, while a simple power-law extrapolation of the optical/UV luminosities of high-z 3C quasars yields $10^{54} < q < 10^{56}$ photon s^{-1} sr^{-1} (Tadhunter 1996a). Thus, for the central source photoionization to work, the ionizing AGN would be required to have a luminosity comparable to the most luminous 3C quasars.

Another way to approach the question of the ionization mechanism is to plot diagnostic line-ratio diagrams (e.g. Robinson et al. 1987). The data for PKS 2250 – 41 are plotted along with the model predictions in Fig. 14. On many of the diagnostic diagrams the data show a good agreement with the predictions of the photoionization models which provide the best fits to the spectra of the EELR around radio galaxies in general. However, the photoionization models run into serious problems explaining the He II(4686)/Hβ diagram: they predict a much higher He II(4686)/Hβ ratio than is observed in the western arc. Notably, the value of He II/Hβ for the central three pixels of the western arc [He II(4686)/H$\beta = 0.08 \pm 0.01$] is more than 10σ below the power-law photoionization prediction, and the discrepancy with the blackbody curve is even higher. It is possible to explain the low He II(4686)/Hβ by invoking an ionizing continuum shape which is considerably harder than those used for the models shown in Fig. 14 (see Binette, Robinson & Courvoisier 1988), but the models would then be inconsistent with the relatively 'normal' He II(4686)/Hβ ratio measured in the nuclear regions.

The photoionization models are also unable to explain the high observed value of the temperature-sensitive [O III] (5007 + 4959)/4363 line ratio in the arc. This is a common problem which has been encountered in the EELR of other active galaxies (Tadhunter et al. 1989b).

Finally, we note that the observed anticorrelation between linewidth and ionization state in the western arc would be difficult to explain in terms of the AGN illuminating the *undisturbed* ambient medium in the host galaxy.

Clearly, our observations cannot be easily reconciled with central source photoionization, and this leads us to consider the alternative: jet-induced shocks.

5.1.2 *Shocks*

In the basic jet/cloud interaction model, the ratio jet drives fast shocks into warm clouds in the ambient interstellar medium. In a variation on this model, Sutherland, Bicknell & Dopita (1993) considered a scenario in which jet-induced instabilities/turbulence leads to the acceleration of discrete clouds of warm gas which subsequently collide, forming shocks. In both of these models, line emission is produced by two distinct mechanisms.

(1) The region directly behind the shock is compressed and heated to very high temperatures ($T \sim 10^{6-7}$ K). As this hot gas cools it emits bremsstrahlung radiation in the form of EUV/X-ray photons until, when the shocked gas has cooled to $T \approx 30\,000$ K, it can emit optical line radiation.

(2) The EUV X-ray continuum from the hot shocked gas photoionizes the cool, dense, post-shock gas (and also the precursor gas ahead of the shock).

There are a number of observational consequences of this model for the EELR. We would expect to find (1) a close association/correlation between the radio and optical emission, (2) line broadening/splitting, possibly high-velocity components in the emission-line spectrum, (3) high temperatures and density enhancement, and (4) a qualitatively different spectrum from that produced by AGN photoionization. These are just the features observed in the western arc of PKS 2250 – 41.

As with the photoionization model, it is important to consider whether the jet-induced shock mechanism is energetically viable. To do this we derive the energy flux from the monochromatic radio power by using the formulae discussed in Bicknell (1995). Following Bicknell, the energy flux (F_E) can be related to the monochromatic radio luminosity P_ν of the lobe by $P_\nu = k_\nu F_E$, where k_ν depends mainly on the age of the source and on the ratio between the lower and upper cut-off Lorentz factors (γ_0 and γ_1) of the electrons. The age of the source can be estimated from steepening of the spectral index. In the case of PKS 2250 – 41, the flux-density measurements from Kuhr et al. (1981) do not show any steepening between 80 MHz and 8 GHz, and a spectral index of 0.92 has been derived from them. We therefore assume a cut-off just above 10 GHz that will represent an upper limit to the age of the radio lobes. The ratio of γ_1/γ_0 can range over a large interval, typically between 10^2 to 10^5 (see discussion in Bicknell 1995), introducing a large uncertainty in our calculations. We have tried to set some constraints on the value of this ratio by using the equipartition magnetic field; the value of γ_1 does, in fact, depend on the magnetic field (again, see Bicknell 1995). The relatively high value of the equipartition magnetic field that we have obtained (75 μG) corresponds to relatively low values for γ_1, and therefore indicates that the most likely value of the ratio γ_1/γ_0 is between 50^2 and 5×10^3. This also represents the most conservative approach. The values of k_ν for the above range of γ_1/γ_0 range between $k_n u \sim 10^{-12}$ and $\sim 0.2 \times 10^{-12}$. For the 5-GHz radio power of the western lobe ($\sim 3.6 \times 10^{33}$ erg s^{-1} Hz^{-1}) we derive a lower limit to the energy flux between $\sim 3.6 \times 10^{45}$ and 1.8×10^{46} erg s^{-1}.

Comparing jet power in PKS 2250 – 41 with the observed emission-line lumionsities,[2] it can be seen that efficiencies of the order of 10^{-2} are needed to convert the bulk kinetic energy of the jet into line emission. Given the nature of the jet/cloud interaction in PKS 2250 – 41, it seems entirely plausible that such an efficiency is possible, and that the jet-induced shocks can provide a substantial fraction of the ionizing energy for the EELR.

The observed variations in the ionization state of the gas across the emission-line nebulosity are also consistent with jet-induced shock models: the ionization-state minimum in the western arc can be explained by the compression of the warm clouds as they enter the shock front – resulting in a lower ionization parameter if the gas is photoionized by the

[2]The observed [O III] luminosity of the arc is $L_{[O\,III]} = 6 \times 10^{42}$ erg s^{-1}, giving an approximate total line luminosity in the arc of $L_{tot} \sim 1.2 \times 10^{44}$ erg s^{-1}; see Tadhunter et al. (1994).

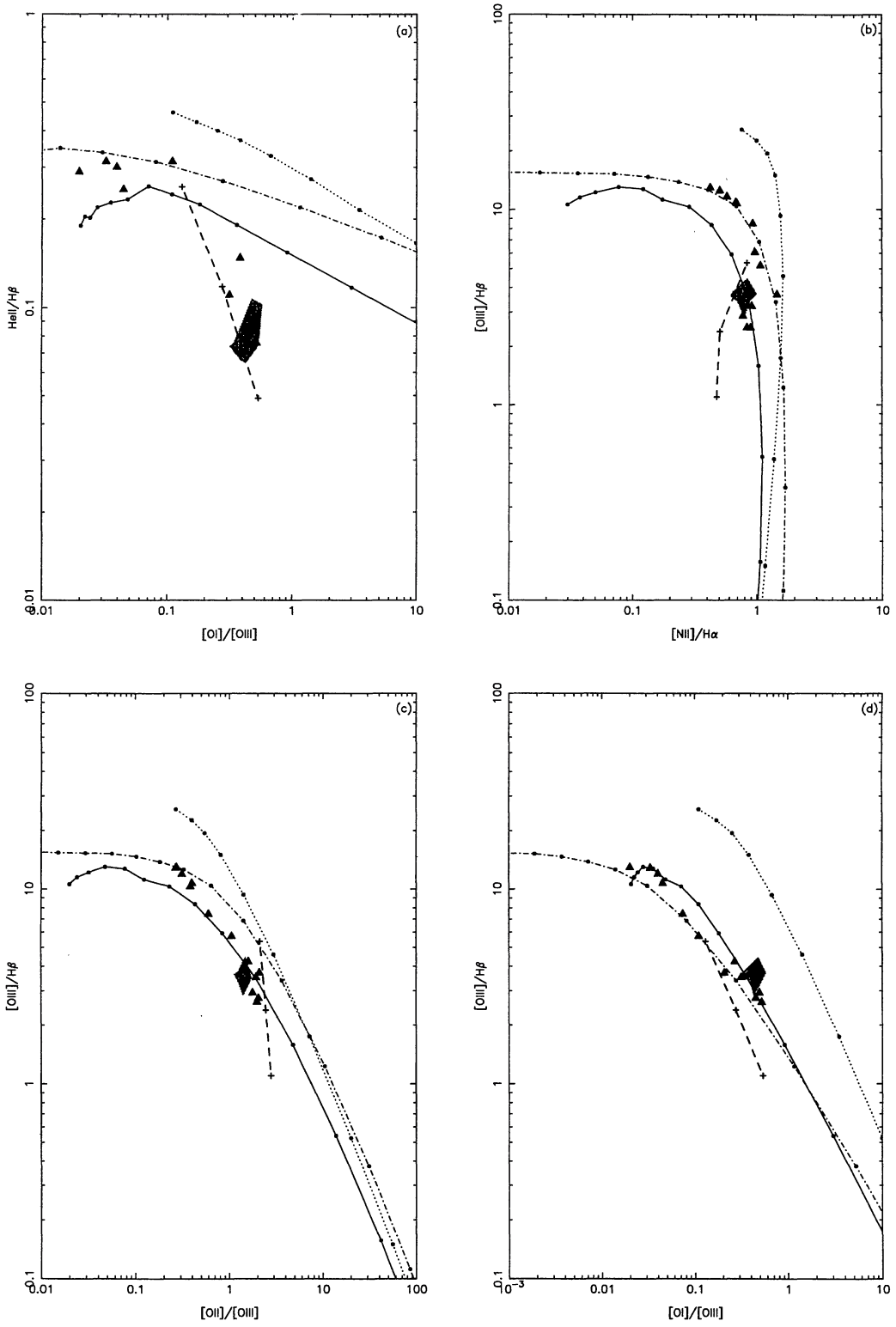

Figure 14. (a) Line ratio diagnostic diagram showing the pixel-by-pixel variations in He II λ4686/Hβ against [O I]/[O III] along the radio axis of PKS 2250 – 41; (b)–(d) show the variation in [O III]/Hβ plotted against the corresponding variations in (b) [N II]/Hα, (c) [O II]/[O III] and (d) [O I]/[O III]. The hollow circles indicate the observed line ratios in the central nuclear region, and the filled triangles represent the line ratios beyond a radius of 1.5 arcec west of the nuclear continuum centroid. The symbols representing the photoionization and shock models are as follows: the solid line represents single-slab power-law photoionization model, $f_\nu \propto \nu^{-1.5}$; the dot-dashed line gives the results for a hot blackbody ($T = 130\,000$ K) ionizing continuum; and the dotted line represents photoionization by the thermal bremsstrahlung emission from a hot (10^7 K) plasma. All the photoionization models are plotted as sequences in the ionization parameter U. The crosses linked by a dashed line indicate single-slab fast shock models of Binette et al. (1985) with shock velocities in the range 116–212 km s^{-1}. The shaded area shows the region occupied by the unequal density cloud–cloud collision models of Sutherland et al. (1993), with velocities in the range 300–450 km s^{-1}.

nucleus – and/or by enhanced shock ionization input associated with radio lobes.

To determine whether the gas is ionized by the jet shocks – and not just compressed – we have plotted the predictions of the fast-shock models of Binette, Dopita & Tuohy (1985) and Sutherland et al. (1993) on the diagnostic diagrams in Fig. 14. For certain shock parameters there is very good agreement with the observed line ratios in the western arc, particularly for the Sutherland et al. model, which agrees at least as well as the photoionization models for all line ratios. The crucial point is that the shock models agree much better with the observed He II(4686)/Hβ and [O III](5007 + 4959)/4363 ratios than the photoionization models.[3]

The emission-line kinematics are also generally consistent with the shock models: large linewidths, such as we observe in the EELR of PKS 2250 – 41, are a natural consequence of material being swept up by the bow shock at the head of a radio jet (e.g. Taylor, Dyson & Axon 1992); with shock models we also expect the line profiles to depend on ionization state, since complex kinematic structures are a natural consequence of fast shocks, and different emission lines will be produced in spatially distinct zones. Indeed, just such kinematic differentiation has been observed in the shocked supernova remnants N49 (Shull 1983) and the Cygnus Loop (Greidanus & Strom 1992).

A possible interpretation of the observed anticorrelation between linewidth and ionization state is that the bulk of the high-ionization [O III] line emission is emitted in the relatively undisturbed precursor zone in front of the shocked region, whereas a larger fraction of the low-ionization line emission comes from the kinematically disturbed cooling zone behind the shock. The different widths of emission lines from different ionic species are then caused by the relative strength of contributions from shocked and unshocked regions. In this case we would expect the Balmer lines to be intermediate in linewidth, because there is substantial emission from both zones, as observed in the western arc of PKS 2250 – 41.

A potential problem in identifying the [O III] with the precursor, however, is that the western arc visible in the [O III] narrow-band image strongly resembles a radiative bow shock, suggesting that the [O III]-emitting gas has already passed through the shock front. Also, the long-slit spectra show that the [O III] lines peak at the same place as the emission from the lower ionization lines and, although the [O III] lines are narrower than the lower ionization lines, they are significantly broadened, with signs of high-velocity components (see Section 4.3.3).

Another possible model to explain the broader low-ionization lines invokes shock-induced acceleration/turbulence in the cooling zone behind the shock. For example, the numerical models of de Young (1986) and Klein, McKee & Colella (1994) exhibit a post-shock vortex in the entrained gas, which would increase the observed velocity dispersion. This model can explain the narrower [O III] lines if the onset of turbulence occurs behind the [O III] zone. This is, of course, an over-simplification – we will still see some low-ionization line emission from the non-turbulent zone and vice-versa. So in this case we would still expect to see a narrow component and a broad component in the line emission, with the relative strengths determined by the ionization state of the line-emitting species.

[3]Although cosmic ray heating (Ferland & Mushotzky 1984) could potentially raise the temperature of the extended gas in PKS 2250 – 41, the measured line ratios are inconsistent with ionization by cosmic rays.

5.2 The origin of the extended emission-line gas

Extended emission-line arc structures, such as those observed in PKS 2250 – 41 do not appear to be a common feature of active galaxies. The only other cases in the literature in which we can find clear evidence for arc features are the powerful radio galaxies 3C 280 (Rigler et al. 1992), 4C 29.30 (van Breugel et al. 1986) and PKS 0634 – 20 (Baum et al. 1988), the LINER galaxy M51 (Cecil 1988), and the Seyfert galaxy Mrk 573 (Pogge & de Robertis 1995). It is significant that, with the possible exception of PKS 0634 – 20, there are strong signs of jet/cloud interactions in all of these objects.

It is important to address the issue of why such arc structures are rare, and the related issue of why the jet/cloud interaction is so spectacular in PKS 2250 – 41.

It has been proposed by some workers that EELR aligned along the radio axes of powerful radio galaxies are the result of jet-induced cooling of a pre-existing hot ISM (de Young 1989; Daly 1992). However, if the gas has condensed out of the hot ISM, then the question arises as to why we do not see this type of structure in the many radio galaxies that show clear evidence for massive hot X-ray haloes (e.g., Cygnus A; Reynolds & Fabian 1996). There are also difficulties with cooling the hot gas, which would start at a temperature of $T \sim 10^7$ K and would then be heated to even higher temperatures by the jet-induced shocks. Given that PKS 2250 – 41 is not in a particularly rich, hot, gaseous environment, it is unlikely that jet-induced cooling of the hot ISM could explain the observed arc structures.

A possible alternative is that the jets are interacting with pre-existing warm/cool gas clouds that represent the remnants of dynamical interactions between galaxies in the associated galaxy group. In support of this theory there is evidence for a companion galaxy to the north-east of the nucleus, which shows signs of a gravitational interaction with PKS 2250 – 41 in the form of tidal tails, as well a close association with the faint eastern arcs. It is also notable that observations of H I in groups of galaxies (van Gorkom 1993) reveal extended (neutral) gas structures with markedly similar morphologies to those we observe in PKS 2250 – 41; the X-ray luminosity of PKS 2250 – 41 is also characteristic of groups of galaxies. The neutral gas strewn about the system by galaxy interactions would present a relatively large 'target' for the radio jets.

If the jets are simply interacting with the gaseous remnants of the galaxy interactions, however, this model does not, by itself, explain the unpolarized blue continuum emission associated with the western arc. Although it has been proposed that the radio jets can promote star formation by compressing warm gas clouds in the haloes of galaxies (de Young 1989; Rees 1989), the problem with this theory for PKS 2250 – 41 is that the peak in the continuum emission in the western arc lies significantly further from the nucleus than either the peak in the line emission or the radio hotspot. This is counter to the standard jet-induced, star-for-

mation model in which the stars are expected to form downstream from the active region at the head of the jet as the gas cools.

The most likely explanation for the spectacular structures observed in PKS 2250 – 41 is that the radio jet is interacting with a neighbouring spiral or irregular galaxy in the associated interacting group. In this case, the observed blue continuum emission represents the integrated light from the stars in the companion. This is supported by the fact that the observed nebular-corrected, broad-band colours and magnitudes are consistent with those observed in Sbc–Sc galaxies. No stellar absorption features are detected, but this is not surprising, given the low signal-to-noise ratios of the current data.

Since spiral galaxies are gas-rich, we would expect to see intense line emission as the radio jet drives shocks into the ISM of the companion. The calculated mass of warm, ionized gas is somewhat less than expected for the H I mass of a late-type spiral galaxy, but it is likely that the *total* gas mass in PKS 2250 – 41, including the gas heated to a hotter phase by the jet/cloud interaction and the remaining H I and molecular gas in the companion, is considerably larger.

In summary, it is likely that the spectacular structures we observe in PKS 2250 – 41 are the consequence a collision between a radio jet and a companion galaxy. The fact that such collisions are likely to be rare would explain why extended emission-line and continuum structures such as we observe in PKS 2250 – 41 are not seen more frequently.

6 CONCLUSIONS

The jet/cloud interaction phenomenon has been recognized for some time. What is new about this study is that our high-quality observations allow us to begin to investigate the physical mechanisms involved at the sites of the interactions and, in particular, to quantify the balance between AGN illumination and jet-induced shocks in the EELR. We arrive at the following conclusions.

Physical conditions. The measured pressure in the western emission-line arc is orders of magnitude higher than expected for the ambient hot ISM at a similar radius in an early-type galaxy or a group of galaxies. This is strong evidence that the ISM in the arc has been compressed by the radio jet.

Ionization mechanisms. The minimum in the ionization state of the gas in the western radio lobe, the anticorrelation between linewidth and ionization state, and the detailed emission-line ratios all support the idea that the ionization state of the gas is strongly influenced by jet shocks. While some of the features might be explained by the compression effect of the shocks even if the clouds are photoionized by a central AGN, the relatively low He II(4686)/Hβ and [O III](5007 + 4959)/4363 ratios provide strong evidence that the jet shocks ionize the EELR directly.

Energetics. For AGN photoionization to work, the central illuminating source would require an ionizing luminosity comparable to the most luminous 3C quasars. On the other hand, only a small fraction of the radio jet bulk power would be required to energize the entire extended emission-line nebulosity.

Kinematics. The relatively broad low-ionization lines and the observed anticorrelation between linewidth and ionization state are inconsistent with AGN illumination of the *undisturbed* ambient medium of the host galaxy. However, such features are not only predicted by shock models, but are actually observed in Galactic supernova remnants.

Overall, the results provide compelling evidence that the jet shocks have a dominant role in defining the ionization, distribution and kinematics of the EELR in this source.

With future higher resolution imaging and spectroscopic observations we will be in an excellent position to model in detail the shocks associated with the jets in PKS 2250 – 41. The results will be particularly relevant to powerful radio galaxies at high redshifts which show many similarities with PKS 2250 – 41.

ACKNOWLEDGMENTS

This paper is based on observations collected at the European Southern Observatory, La Silla, Chile, the Anglo-Australian Observatory, Siding Spring, Australia and the Australia Telescope Compact Array (ATCA), which is operated by the CSIRO Australia Telescope National Facility. We are grateful to Richard McMahon for providing accurate positions of stars in the field of PKS 2250 – 41. CNT thanks Evert Meurs and the Dublin Institute of Advanced Studies for their hospitality during a stay at Dunsink Observatory, in the course of which part of the paper was writen. NEC and MAS acknowledge financial support from PPARC. We also thank the Starlink project for support of our computer facilities.

REFERENCES

Bartel P. D., 1989, ApJ, 336, 606
Baum S. A., Heckman T. M., 1989, ApJ, 336, 681
Baum S. A., Heckman T. M., Bridle A., van Breugel W. J. M., Miley G. K., 1988, ApJS, 68, 643
Bicknell G., 1995, ApJS, 101, 29
Binette L., Dopita M. A., Tuohy I. R., 1985, ApJ, 297, 476
Binette L., Robinson A., Courvoisier T. J.-L., 1988, A&A, 190, 29
Blandford R., Rees M., 1974, MNRAS, 169, 395
Cecil G., 1988, ApJ, 329, 38
Chambers K. C., Miley G. K., van Breugel W. J. M., 1990, ApJ, 363, 21
Cimatti A., di Serego Alighieri S., Fosbury R. A. E., Salvati M., Taylor D., 1993, MNRAS, 264, 421
Clark B. G., 1980, A&A, 89, 377
Daly R. A., 1990, ApJ, 355, 416
de Robertis M. M., Osterbrock D. E., 1984, ApJ, 286, 171
de Young D. S., 1986, ApJ, 307, 62
de Young D. S., 1989, ApJ, 342, L59
Dickson R., Tadhunter C. N., Shaw M. A., Clark N. E., Morganti R., 1995, MNRAS, 273, L29
Djorgovski S., Spinrad H., Pedelty J., Rudnick L., Stockton A., 1987, AJ, 93, 6
Duncan R. A., Sproats L. N., 1993, Proc. Astron. Soc. Aust., 10, 16
Fabian A. C., 1989, MNRAS, 238, 41P
Ferland G. J., Mushotzky R. F., 1984, ApJ, 286, 42
Fosbury R. A. E., 1989, in Meurs E. J. A., Fosbury R. A. E., eds, ESO Workshop on Extranuclear Activity in Galaxies. ESO Scientific Publications, p. 169

Greidanus H., Strom R. G., 1992, A&A, 257, 265
Högbom J., 1974, A&AS, 15, 417
Hook R. N., Lucy L. B., 1993, ST-ECF Newsletter, 19, 6
Jackson N., Sparks W. B., Miley G. K., Macchetto F., 1993, A&A, 269, 128
Klein R., McKee C., Colella P., 1994, ApJ, 420, 213
Kuhr h., Witzel A., Pauliny-Toth I. I. K., Nauber U., 1981, A&AS, 45, 367
Liu R., Pooley G., 1991, MNRAS, 249, 343
Lucy L. B., 1974, AJ, 79, 745
McCarthy P. J., van Breugel W. J. M., Spinrad H., Djorgovski S., 1987, ApJ, 321, L29
McCarthy P. J., Spinrad H., van Breugel W. J. M., Liebert J., Dickinson M., Djorgovski S., Eisenhardt P., 1990, ApJ, 365, 487
McCarthy P. J., Baum S., Spinrad H., 1996, ApJS, in press
Miley G. K., Chambers K. C., van Breugel W. J. M., Macchetto F., 1992, ApJ, 401, L69
Morganti R., Robinson A., Fosbury R. A. E., di Serego Alighieri S., Tadhunter C. N., Malin D. F., 1991, MNRAS, 249, 91
Morganti R., Killeen N. E. B., Tadhunter C. N., 1993, MNRAS, 263, 1023
Osterbrock D. E., 1989, The Astrophysics of Gaseous Nebulae and Active Galactic Nuclei. University Science Books
Pacholczyk A. G., 1970, Radio Astrophysics. Freeman, San Francisco
Penston M. A. et al., 1990, A&A, 236, 53
Pogge R. W., de Robertis M. M., 1995, ApJ, 451, 585
Ponman T. J., Allan D. J., Jones L. R., Merrifield M., McHardy I. M., Lehto H. J., Luppino G. A., 1994, Nat, 369, 462
Rees M. J., 1989, MNRAS, 239, 1P
Reynolds C. S., Fabian A. C., 1996, MNRAS, 278, 479
Richardson B. H., 1972, J. Opt. Soc. Am, 62, 55
Rigler M. A., Lilly S. J., Stockton A., Hammer F., Le Fèvre O., 1992, ApJ, 385, 61
Robinson A., Binette L., Fosbury R. A. E., Tadhunter C. N., 1987, MNRAS, 227, 97
Sault R. J., Teuben P. J., Wright M. C. H., 1995, in Shaw R., Payne H. E., Hayes J. J. E., eds, ASP Conf. Ser. Vol. 77, Astronomical Data Analysis Software and Systems IV. Astron. Soc. Pac., San Francisco, p. 433
Schwab F. R., 1980, Proc. SPIE, 231, 18
Shaw M. A., Tadhunter C. N., Dickson R., Morganti R., 1995, MNRAS, 275, 703
Shul P., 1983, ApJ, 275, 611
Simard-Normandin M., Kronberg P., 1980, ApJ, 242, 74
Sutherland R. S., Bicknell G. V., Dopita M. A., 1993, ApJ, 414, 510
Tadhunter C. N., 1987, D.Phil. thesis, Univ. Sussex
Tadhunter C. N., 1991, MNRAS, 251, 46P
Tadhunter C. N., 1996a, in Carilli C. L., Harris D. E., eds, Cygnus A – Study of a Radio Galaxy. Cambridge Univ. Press, Cambridge, p. 33
Tadhunter C. N., 1996b, in Ekers R., Fanti C., Padrielli C., eds, Proc. IAU Symp. 175, Extragalactic Radio Sources. Kluwer, Dordrecht, p. 217
Tadhunter C. N., Fosbury R. A. E., di Serego Alighieri S., Bland J., Danziger I. J., Goss W. M., McAdam W. B., Snijders M. A. J., 1988a, MNRAS, 235, 403
Tadhunter C. N., Fosbury R. A. E., di Serego Alighieri S., 1988b, in Maraschi L., Maccacaro T., Ulrich M.-H., eds, BL Lac Objects. Proc. Como Conf. Springer-Verlag, Berlin, p. 79
Tadhunter C. N., Fosbury R. A. E., Quinn P., 1989a, MNRAS, 240, 225
Tadhunter C. N., Robinson A., Morganti R., 1989b, in Fosbury R. A. E., Meurs E. J. A., eds, Extranuclear Activity in Galaxies. ESO Scientific Publications, p. 293
Tadhunter C. N., Scarrott S. M., Draper P., Rolph C., 1992, MNRAS, 256, 53P
Tadhunter C. N., Morganti R., di Serego Alighieri S., Fosbury R. A. E., Danziger I. J., 1993, MNRAS, 263, 999
Tadhunter C. N., Metz S., Robinson A., 1994a, MNRAS, 268, 989
Tadhunter C. N., Shaw M. A., Clark N. E., Morganti R., 1994b, A&A, 288, L21
Taylor D., Dyson J. E., Axon D. J., 1992, MNRAS, 255, 351
van Breugel W. J. M., Miley G. K., Heckman T. H., Butcher H. R., Bridle A. H., 1985, ApJ, 290, 496
van Breugel W. J. M., Heckman T. M., Miley G. K., Filippenko A., 1986, ApJ, 311, 58
van Gorkom J., 1993, in Shull J. M., Thronson H. A. Jr., eds, The Environment and Evolution of Galaxies. Kluwer, Dordrecht, p. 345